CDF/ANAL/ELECTROWEAK/CDFR/10075
17 Oct 2010

QCD Corrections to Drell-Yan Lepton Angular Distributions

J.-Y. Han, A. Bodek, Y.S. Chung, K.S. McFarland, and W.K. Sakumoto
University of Rochester

ABSTRACT

Charged Drell-Yan lepton pairs are produced in the process, $p\bar{p} \rightarrow \gamma^* Z + X$, with the subsequent decay of the γ^*/Z into lepton pairs (l^+l^-). In general, the angular distribution of the l^+ can be a function of s, the γ^*/Z mass (Q^2), rapidity (y), and the transverse momentum (P_{T}). We study the P_{T} dependence of the angular distribution using 2.1 fb^{-1} of CDF Run II data, and compare to the CDF Monte Carlo and other theory predictions.

1 Theory

The parton level differential cross sections for dilepton pair production (e.g. Drell-Yan, $Z's$ or $W's$) for $q\bar{q}$ annihilation can be written as

$$\frac{d\sigma}{d(\ cos\theta)} = C\left[(1+cos^2\theta) + B\ cos\theta\right] \tag{1}$$

where θ is the emission angle of the positive charged lepton relative to the quark momentum in the center of mass frame. For W and Z bosons B is a parameter that depend on the weak isospin and charge of the incoming fermions (B=2 for W bosons). The cross sections for forward events (σ_f) and backward events (σ_b) are given by

$$\begin{aligned} \sigma_f &= \int_0^1 \frac{d\sigma}{d(\ cos\theta)} d(\ cos\theta) \quad (2) \\ &= C\left[\left(1+\frac{1}{3}\right) + B\left(\frac{1}{2}\right)\right] \\ \sigma_b &= \int_{-1}^0 \frac{d\sigma}{d(\ cos\theta)} d(\ cos\theta) \quad (3) \\ &= C\left[\left(1+\frac{1}{3}\right) - B\left(\frac{1}{2}\right)\right] \end{aligned}$$

The electroweak interaction introduces the asymmetry (a linear dependence on $cos\theta$), which can be expressed as

$$A_{fb}^{total} = \frac{\sigma_f - \sigma_b}{\sigma_b + \sigma_b} = \frac{3}{8}B \tag{4}$$

The total differential cross sections dilepton pair production (e.g. Drell-Yan, $Z's$ or $W's$) for proton-antiproton annihilation [1, 2, 3, 4, 5] is given by a modified equation:

$$\begin{aligned} \frac{d\sigma}{dP_T^2 dy d\cos\theta d\phi} &= C[(1+\cos^2\theta) \\ &+ \frac{1}{2}A_0(1-3\cos^2\theta) + A_1\sin 2\theta\cos\phi \\ &+ \frac{1}{2}A_2\sin^2\theta\cos 2\phi + A_3\sin\theta\cos\phi \\ &+ A_4 B\cos\theta + A_5\sin^2\theta\sin 2\phi \\ &+ A_6\sin 2\theta\sin\phi + A_7\sin\theta\sin\phi] \end{aligned} \tag{5}$$

where P_T and y are the transverse momentum and the rapidity of the *dilepton* in the lab frame and θ and ϕ are the polar and azimuthal angles of the charged lepton from the *dilepton* decay in the Collins-Soper (CS) frame [20].

When integrated over all ϕ the differential cross section reduces to:

$$\frac{d\sigma}{dP_T^2 dy d\cos\theta} = C[(1+\cos^2\theta) + \frac{1}{2}A_0(1-3\cos^2\theta) + A_4 B\cos\theta] \tag{6}$$

When integrated over all $\cos\theta$ the differential cross section reduces to:

$$\frac{d\sigma}{dP_T^2 dy d\phi} = C[1 + \frac{3\pi A_3}{16}\cos\phi + \frac{A_2}{4}\cos 2\phi + \frac{3\pi A_7}{16}\sin\phi + \frac{A_5}{4}\sin 2\phi] \tag{7}$$

where the angular coefficients, A_5 and A_7, are close to zero.

The parameters A_0, A_2 and A_4 are non-zero for finite values of P_T. For the $q\bar{q}$ process ($q+\bar{q} \rightarrow \gamma^*/Z+g$), the non-zero transverse momentum originates from gluon emission by the $q\bar{q}$ initial state. For the qg process ($q+g \rightarrow \gamma^*/Z+q$), the boson P_T originates from a non-zero transverse momentum recoil of the quark in the final state.

For the $q\bar{q}$ process, perturbative calculations (simple derivation is given in Appendix B) show [6] that the coefficients A0, A2 and A4[9] are independent of y and independent of the parton distribution functions. They originate from pure kinematics and are related to ξ , which is the angle of the proton (antiproton) beam in the Collins-Soper frame as follows:

$$\begin{aligned} A_0^{q\bar{q}} &= A_2^{q\bar{q}} = sin^2\,\xi = \frac{P_T^2}{P_T^2 + M_{\ell\ell}^2} \\ A_4^{q\bar{q}} &= cos\ \xi = \frac{M_{\ell\ell}}{(P_T^2 + M_{\ell\ell}^2)^{1/2}} \end{aligned} \tag{8}$$

For the $q\bar{q}$ process, the above relations remain the same in resummation calculations [7]. On the other hand, the qg the process is changed by higher order QCD corrections.

Theory calculation[8] show that for boson production at the Tevatron the qg process is much smaller than $q\bar{q}$ to Z gluon process. Therefore, the angular distribution coefficients should be close to what is given in Eq. 9.

For reference we present other notations that is used in the literature. If we sum up negative and positive values of $cos\theta$ and integrate over ϕ some papers use:

$$\frac{d\sigma}{dP_T^2 dy d\cos\theta} = C(1 + \frac{A_0}{2})[1 + \alpha_2 \cos^2\theta + \alpha_1 \cos\theta] \tag{9}$$

where

$$\alpha_2 = \lambda = \frac{2 - 3A_0}{2 + A_0}, \qquad A_0 = \frac{2(1-\lambda)}{3+\lambda}, \qquad \alpha_1 = \frac{2BA_4}{2 + A_0}$$

and also

$$\frac{d\sigma}{dP_T^2 dy d\cos\theta d\phi} = C'(\frac{1}{\lambda+3})[1 + \lambda\cos^2\theta + \mu\ sin2\theta\cos\phi + \frac{\nu}{2}\sin^2\theta\cos 2\phi] \tag{10}$$

$$\lambda = \frac{2 - 3A_0}{2 + A_0}, \qquad \mu = \frac{2A_1}{2 + A_0}, \qquad \nu = \frac{2A_2}{2 + A_0}$$

And we integrate over $cos\theta$, some papers use:

$$\frac{d\sigma}{dP_T^2 dy d\phi} = C''[1 + \beta_1\cos\phi + \beta_2\cos 2\phi + \beta_3\sin\phi + \beta_4\sin 2\phi] \tag{11}$$

where

$$\beta_1 = \frac{3\pi A_3}{16}, \quad \beta_2 = \frac{A_2}{4}, \beta_3 = \frac{3\pi A_7}{16}, \quad \beta_4 = \frac{A_5}{4}$$

The relation $A_0 = A_2$ which is equivalent to $1 - \lambda - \nu = 0$, is known as the Lam-Tung(LT) relation. It is valid to all orders for the $q\bar{q}$.

At LO it was shown that it is still true(including qg) for the sum of $q\bar{q}$ and qg contributions [2, 3]. However, the qg diagram at higher orders leads to a violation of the LT relation[2, 3] (it makes A_2 somewhat smaller than A_0. The angular coefficient A_0 for the qg diagram was calculated in LO by Linfors in 1979 publication, [10].

If we define $r = P_T M_{\ell\ell}$ then A_0 for the qg is given by:

$$A_0^{qg} = \frac{r^2}{1+r^2} \times \frac{5}{1 + 2[1 - \frac{1}{(1+r^2)})^{1/2}]^2} \tag{12}$$

Which implies that at small values of r ($=P_T M_{\ell\ell}$) the angular coefficient $A_0^{qg} = 5A_0^{q\bar{q}}$, and at very large values of r the angular coefficient $A_0^{qg} = \frac{5}{3}A_0^{q\bar{q}}$. Since the fraction of the contributions of the qg and $q\bar{q}$ diagrams is a function of the rapidity y, this implies that $A_0^{qg+q\bar{q}}$ will depend on y. Deviations of the measured values of

A_0 from the prediction $A_0^{q\bar{q}} = \frac{r^2}{1+r^2}$ would be evidence for the contribution from the gq diagram (which is expected to be small for Z production at the Tevatron, but larger for Z boson production at the LHC, and also larger for W production at the Tevatron). Since $A_0^{qg+q\bar{q}} = A_2^{qg+q\bar{q}}$ in leading order, deviations from the Lam-Tung relations $A_2 = A_0$ would imply both, a contribution from the gq diagram and also from higher order QCD terms.

In the remainder of this paper we will use the notation A_0, A_2, A_3 and $A_4 \equiv A_4 B$.

This CDF note has the main measurement part, part1, and several Appendixs. In part 1 we focus on checking if the angular distribution in the CDF PYTHIA Monte Carlo is in agreement with our data. The primary reason for this check is to make sure that our acceptance calculation for the measurement of the rapidity distribution of dilepton pairs in the Z boson region ($66 < M_{ee} < 116$ GeV) is correct. We have checked that the Monte Carlo is in agreement with the P_T distributions, and also tuned it to agree with our measured rapidity distribution. A check of the angular distribution is the final check on the validity of our acceptance calculation.

Experimentally, the P_T of the dilepton (and therefore its measured angular distribution) can originate from either initial state radiation (as calculated in several QCD models) or from final state photon radiation. To concentrate on QCD effect and compare the measurement with QCD theories, we want to compare the measured angular distribution to the QCD predictions before final state photon radiation.

We also cross checke the measurement with the tighter mass window which minimizes the final state photon radiation (even thought the measurement is performed in QED born level which is before QED radiation). The measurement with the tight mass window is described in Appendix A.

In part 1, which is focused on the check of the acceptance, we use the full mass range ($66 < M_{ee} < 116$ GeV), which is the mass region for our measurement of the Z boson rapidity distribution.

2 Part 1: $d\sigma/dy$ Analysis and Extention for Angular Distributions

2.1 Introduction

The acceptance for Drell-Yan dilepton pairs is obtained using the Monte Carlo event generator, PYTHIA [11], and CDF detector simulation programs. PYTHIA generates the hard, leading order (LO) QCD interaction, $q + \bar{q} \rightarrow \gamma^*/Z$ (or $q + \bar{q}' \rightarrow W$), simulates initial state QCD radiation via its parton shower algorithms, and generates the decay, $\gamma^*/Z \rightarrow l^+l^-$ (or $W \rightarrow l\nu$). The CTEQ5L [13] nucleon parton distribution functions (PDFs) are used in the QCD calculations. The intermediate vector boson P_{T} is tuned to CDF's Run I measurement of the fully corrected $d\sigma/dP_{\mathrm{T}}$ of ee pairs in the mass region $66 < M_{ee} < 116$ GeV [14]. PYTHIA with parton showering is a QCD resummation calculation Monte Carlo. The usual QCD resummation calculations are: RESBOS [18] (resummation in impact parameter space) and VBP [19] (resummation in P_{T} space).

The rapidity distribution, $d\sigma/dy$, for $\gamma^*/Z \to ee$ events produced in $p\bar{p}$ collisions at $\sqrt{s} = 1.96$ TeV has been measured [15, 16] for ee pairs in the 66–116 GeV mass range. Using the same data used in the Run II rapidity measurement, we examine the e^+ angular distribution versus the γ^*/Z $P_{\rm T}$ and compare it against PYTHIA predictions. The Drell-Yan angular distribution is measured in the Collins-Soper [20], center-of-momentum (CM), rest frame of the dileptons. The polar angle is denoted as θ and the azimuthal angle, ϕ. The Collins-Soper rest frame axes are completely specified by the 4–momenta of the two leptons in the $p\bar{p}$ CM frame.

In this part 1 of note, we focus on the comparison of the measured $\cos\theta$ and ϕ distribution with CDF PYTHIA MC events that are put through CDF detector simulation and treated exactly as the data (e.g., trigger simulation and analysis cuts) for several bins of boson $P_{\rm T}$. This comparison tests if the CDF PYTHIA MC reproduce the data. By tweaking the CDF PYTHIA's $\cos\theta$ or ϕ distribution to get the best match with the data, the tweaked $\cos\theta$ or ϕ distribution provides a measurement of the true $\cos\theta$ or ϕ distribution.

2.2 QCD Calculations for Angular Distributions

Various calculations are used for the $\cos\theta$ and ϕ predictions: PYTHIA, VBP, RESBOS, MADGRAPH, PHOWEG, PYTHIA+1jet, DYRAD and FEWZ. These are QCD resummation calculations or QCD calculations in the fixed order perturbation theories. The VBP prediction uses a QCD NLO QCD matrix element for the γ^*/Z production and it has no QED radiation. We find that PYTHIA with no QED final state radiation (FSR) and VBP give similar results for A_0 and A_2, which follows the approximation of $q\bar{q}$ annihilation process, $A_0 = A_2 = \frac{P_{\rm T}^2}{P_{\rm T}^2 + M_{\ell\ell}^2}$. The higher QCD order predictions like MADGRAPH, PHOWEG, PYTHIA+1jet, DYRAD, and FEWZ are close and has higher A_0 and A_2 in high $P_{\rm T}$ ($P_{\rm T} > 35$) than PYTHIA by up to $\sim 50\%$. The QCD resummation calculation in impact parameter space, RESBOS, has the similar result with PYTHIA in low $P_{\rm T}$ region, $P_{\rm T} < 30$ and cross over to the higher QCD order predictions in high $P_{\rm T}$ region for A_0 and A_2.

The default PYTHIA $\gamma^*/Z \to ee$ (MSEL=11) uses a LO matrix element ($Z + 0$ jet) and parton showering produces the boson $P_{\rm T}$. PYTHIA's can also do the NLO $Z+1$ jet (MSEL=13), but to avoid double counting, it is used only at large boson $P_{\rm T}$. The standard CDF $\gamma^*/Z \to ee$ simulated data sets use PYTHIA's MSEL=11 event generator with the CDF underlying event "Tune A" and PYTHIA's QED parton showering (which uses the same machinery as QCD parton showering aside from coupling differences). We will refer to this standard version as CDF PYTHIA (CDF PYTHIA always includes QED).

The QED final state radiation has an effect at low boson $P_{\rm T}$. To determine the contribution of this QED radiation, we use PYTHIA's MSEL=11 event generator with PYTHIA's QED FSR turned off (MSTJ(41)=1) and with the underlying event "Tune A" turned off. The "Tune A" is turned off to speed up event generation. We refer to this version with this shorthand notation: PYTHIA'(no QED).

Both the standard CDF PYTHIA $\gamma^*/Z \to ee$ simulated data sets and the one

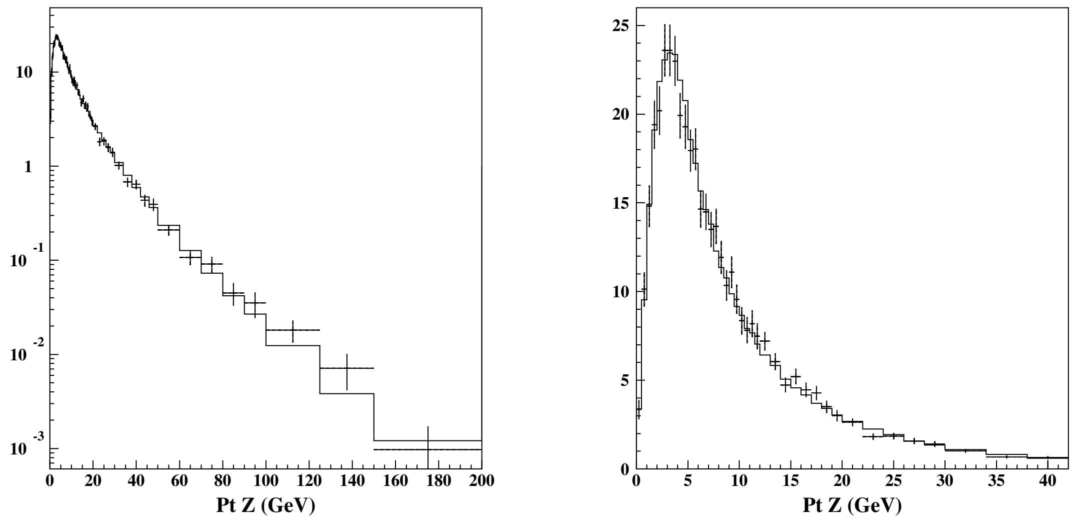

Figure 1: Tuned CDF PYTHIA 6.21 $d\sigma/dP_{\mathrm{T}}$ of ee pairs in the mass region $66 < M_{ee} < 116$ vs P_{T}. The Run I measurement is the crosses, and the histogram, PYTHIA. The y axis is $d\sigma/dP_{\mathrm{T}}$, in pb per GeV/c. The two plots have identical content and are just displayed differently.

without QED FSR use the CDF γ^*/Z P_{T} tuning parameters [21].

CDF PYTHIA and PYTHIA (no QED) as well as VBP's azimuthally integrated $\cos\theta$ distributions (in the P_{T} bins considered) can all be fit well by the following functional form,w

$$f(x) = (1 + x^2) + A_0 \cdot (1 - 3x^2)/2 + A_4 \cdot x \tag{13}$$

here $x = \cos\theta$. Over the interval $-1 < x < 1$, 1, x, and $(1 - 3x^2)/2$ are the Legendre polynomials, $P_0(x)$, $P_1(x)$, and $P_2(x)$.

The ϕ distribution is also fit well by the following functional form,

$$f(\phi) = 1 + \frac{3\pi A_3}{16}\cos\phi + \frac{A_2}{4}\cos 2\phi \tag{14}$$

here we ignore A_5 and A_7 since these two coefficients are expected to be close to zero.

The fits for the MC A_0 and A_4 extracted from fits to the CDF PYTHIA $\cos\theta$ MC distribution in various boson P_{T} bins are given in Table 1. The "A_0 CDFmc" and "A_4 CDFmc" columns in this table are for the CDF standard MC sample. The corresponding A_0(no QED) and A_4(no QED) columns are from PYTHIA with QED FSR turned off. The corresponding fits for A_0 (VBP) and A_4 (VBP) to the P_{T}–space resummation from the VBP $\cos\theta$ distribution (as a function of boson P_{T}) and also A_2 (VBP) and A_3 (VBP) from the ϕ distribution are given in Table 2.

The corresponding fits for A_0, A_4, A_2, and A_3 to the b–space resummation ResBos $\cos\theta$ or ϕ distribution for various boson P_{T} bins are given in Table 3. For these

$P_{\rm T}$ bin (GeV)	A_0(*no QED*)	A_4(*no QED*)	A_0 CDFmc	A_4 CDFmc
00–05 (2.9)	$(.188 \pm .343)10^{-2}$	$.112 \pm .003$	$(.377 \pm .016)10^{-1}$	$.112 \pm .001$
05–10 (7.2)	$(.142 \pm .033)10^{-1}$	$.113 \pm .003$	$(.438 \pm .018)10^{-1}$	$.110 \pm .001$
10–20 (14.1)	$(.227 \pm .034)10^{-1}$	$.113 \pm .003$	$(.554 \pm .020)10^{-1}$	$.112 \pm .002$
20–40 (27.5)	$(.770 \pm .034)10^{-1}$	$.117 \pm .003$	$.108 \pm .003$	$.115 \pm .002$
40–60 (48.0)	$.202 \pm .006$	$.116 \pm .005$	$.218 \pm .006$	$.125 \pm .004$
60–80 (68.2)	$.346 \pm .011$	$.120 \pm .008$	$.362 \pm .010$	$.122 \pm .008$
> 80 (97.7)	$.528 \pm .014$	$.102 \pm .011$	$.555 \pm .013$	$.094 \pm .010$
> 40 (57.9)	$.272 \pm .005$	$.115 \pm .004$	$.290 \pm .005$	$.120 \pm .004$
	$.426 \pm .005^{*}$	$.110 \pm .004^{*}$	N/A	N/A

Table 1: Mass region $66 < M_{ee} < 116$. Fit parameters to CDF PYTHIA's MC azimuthally integrated $\cos\theta$ distribution for various $P_{\rm T}$ bins. In the "$P_{\rm T}$ bin" column, the number in parenthesis is the mean $P_{\rm T}$ in the bin. The A_0 CDFmc and A_4 CDF mc columns are the fits for the CDF PYTHIA standard MC sample which includes QED. The A_0 (no QED) and A_4 (no QED) are for PYTHIA without QED FSR. The > 40 GeV row, the * numbers are for the PYTHIA $Z + 1$ jet event sample.

$P_{\rm T}$ (GeV)	A_0(VBP)	A_4(VBP)	A_2(VBP)	A_3(VBP)
00–05	$(.392 \pm .094)10^{-2}$	$.117 \pm .001$	$(.098 \pm .288)10^{-2}$	$(.008 \pm .122)10^{-2}$
05–10	$(.894 \pm .093)10^{-2}$	$.122 \pm .001$	$(.808 \pm .248)10^{-2}$	$(-.009 \pm .105)10^{-2}$
10–20	$(.281 \pm .009)10^{-1}$	$.125 \pm .001$	$(.271 \pm .023)10^{-1}$	$(-.285 \pm .980)10^{-3}$
20–30	$(.710 \pm .008)10^{-1}$	$.127 \pm .001$	$(.700 \pm .023)10^{-1}$	$(-.259 \pm .989)10^{-3}$
30–40	$.126 \pm .001$	$.128 \pm .001$	$.124 \pm .002$	$(-.004 \pm .102)10^{-2}$
40–60	$.209 \pm .001$	$.127 \pm .001$	$.207 \pm .003$	$(-.032 \pm .109)10^{-2}$
60–80	$.337 \pm .001$	$.123 \pm .001$	$.333 \pm .004$	$(-.030 \pm .170)10^{-2}$

Table 2: Mass region $66 < M_{ee} < 116$. Fit parameters to VBP's azimuthally integrated $\cos\theta$ or ϕ distribution for various $P_{\rm T}$ bins. The VBP QCD calculation does not include QED initial or final state radiation.

P_T bin (GeV)	A_0	A_4	A_2	A_3
00–05	$(.319 \pm .181)10^{-2}$	$.112 \pm .001$	$(.474 \pm .332)10^{-2}$	$(-.077 \pm .141)10^{-2}$
05–10	$(.114 \pm .019)10^{-1}$	$.116 \pm .001$	$(.103 \pm .034)10^{-1}$	$(-.422 \pm .144)10^{-2}$
10–20	$(.257 \pm .025)10^{-1}$	$.119 \pm .002$	$(.242 \pm .046)10^{-1}$	$(-.760 \pm .198)10^{-2}$
20–30	$(.706 \pm .018)10^{-1}$	$.120 \pm .001$	$(.695 \pm .033)10^{-1}$	$(-.740 \pm .142)10^{-2}$
30–40	$.129 \pm .002$	$.124 \pm .002$	$.133 \pm .004$	$(-.104 \pm .015)10^{-1}$
40–60	$.248 \pm .002$	$.122 \pm .002$	$.258 \pm .004$	$(-.181 \pm .016)10^{-1}$
60–80	$.503 \pm .003$	$.109 \pm .002$	$.513 \pm .005$	$(-.357 \pm .023)10^{-1}$

Table 3: Mass region $66 < M_{ee} < 116$. Fit parameters to ResBos's azimuthally integrated $\cos\theta$ and ϕ distribution for various P_T bins. The ResBos calculation does not include QED initial or final state radaition.

ResBos calculations, the unweighted event generator mode is used, both resummed and perturbative pieces are included, and separate runs for the u– and d–type quark flux grid files are required. As the total cross sections for the u– and d–type quark flux grid files are different for the various boson P_T bins, the separate runs are normalized to the same luminosity before combination.

For large boson P_T, PYTHIA's $Z+1$ jet matrix element event generator (MSEL = 13) without any parton showering (MSTP(61) = 0 and MSTJ(41) = 0) is used to evaluate the NLO angular coefficients, A_0, A_4, A_2, and A_3. PYTHIA 6.4 [12] is used with CTEQ6M [22] PDFs. The results for the $P_T > 30$ GeV bins are as follows.

P_T (GeV)	A_0	A_4	A_2	A_3
30–40	$.221 \pm .005$	$.111 \pm .004$	$.217 \pm .009$	$(.813 \pm .385)10^{-2}$
40–60	$.348 \pm .005$	$.106 \pm .004$	$.341 \pm .009$	$(-.567 \pm .387)10^{-2}$
60–80	$.501 \pm .005$	$.099 \pm .004$	$.491 \pm .009$	$(-.330 \pm .390)10^{-2}$
>80	$.668 \pm .005$	$.085 \pm .004$	$.661 \pm .009$	$(-.102 \pm .039)10^{-1}$

The number in parenthesis in the P_T bin column is the mean P_T in that bin. If QCD parton showering is turned on for the P_T 20–40 GeV bin, the shift is small: $A_0 = .149 \pm .005$ and $A_4 = .119 \pm .004$.

Other predictions including the predictions described in this section are compared with the measurement as a function of P_T which is shown in Figure 13 and 14.

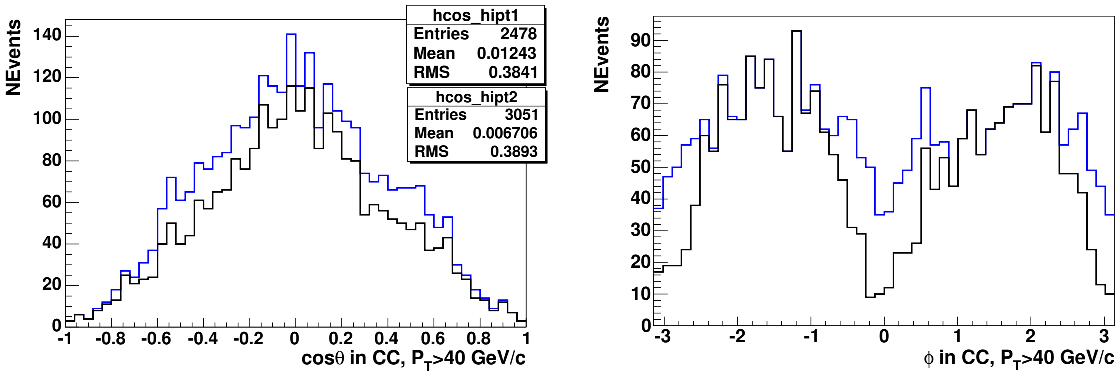

Figure 2: $\cos\theta$ and ϕ distribution of the data in Z $P_T > 40\ GeV/c^2$(CC topology). The blue histograms have the symmetric $E_T > 25\ GeV$ cut on both legs and the black histograms have $E_T > 25\ GeV$ cut for the higher E_T leg and $E_T > 15\ GeV$ cut for the lower E_T leg.

2.3 The Data

The data collected by CDF Run II during 2004–2007 is used to compare to the angular distribution of PYTHIA generator. The integrated luminosity consists of 2.1 fb^{-1} after a good run requirement. The two electrons are selected to reconstruct γ^*/Z boson in $66 < M_{ee} < 116$ GeV. The dielectron sample consists of three different e^+e^- pair topologies. The CC topology has both electrons in the central calorimeter with $|\eta| < 1.1$. The CP topology has one electron in the central calorimeter with $|\eta| < 1.1$, and another in the plug calorimeter with $1.2 < |\eta| < 2.8$. The PP topology has both electrons in the plug calorimeter with $1.2 < |\eta| < 2.8$. The electron identification and event selections are required to clean up the sample and the selection criteria is described in [16]. The selection criteria is almost same with the differential cross section of the rapidity measurement [16] except two things. One is the electron E_T cut in CC topology. At high Z P_T and $\phi \sim 0$ or π, one electron has high E_T and another has very soft E_T. The symmetric $E_T > 25\ GeV$ cut on both legs rejects the events since the soft E_T leg cannot pass E_T selection. The region of $\phi \sim 0$ or π in high Z P_T has lower acceptance in this reason, so we release the E_T cut of the lower E_T leg to get more acceptance in the region. The CC topology is very clean sample (background rate is less than 0.3% level), so not much background comes in even though E_T cut releasing. Therefore, we release E_T cut of the lower E_T leg up to 15 GeV, which increases the acceptance by $\sim 23\%$ and makes ϕ distribution flatter in $P_T > 40\ GeV/c^2$. Figure 2 shows the acceptanced events changes in $\cos\theta$ and ϕ from E_T cut release.

The second change is the track requirement in the plug leg. In $d\sigma/dy$ analysis, the CP topology has a track requirement only in the central leg and the PP topology is required to have at least one track of two electrons to increase the acceptance in high rapidity region. However, the background level is higher in high P_T region, more than 7% level, so we need to reduce the background in high P_T region requiring

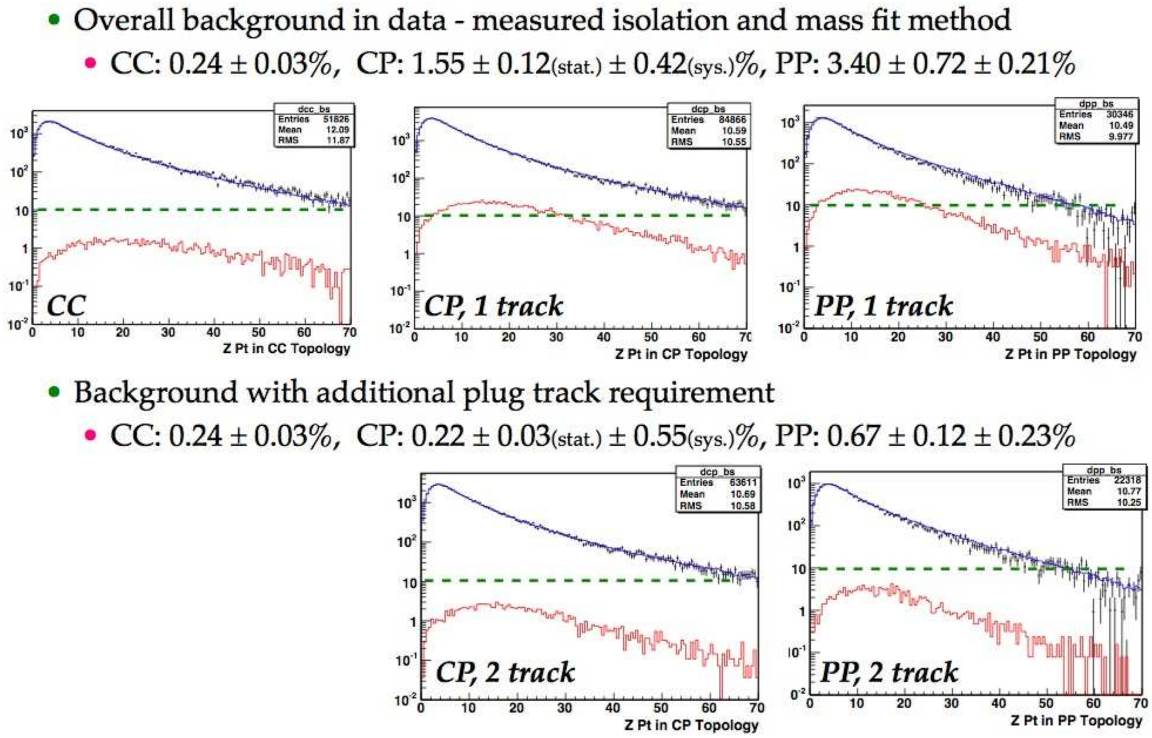

Figure 3: The top three plots are Z P_T distribution of each topology with the event selection of $d\sigma/dy$ analysis. (CP and PP topologies have one and more track events.) The bottom plots correspond to two track events for CP and PP topology. The black points are data, the blue histogram is Pythia MC prediction, and the red histogram is QCD background. The QCD background is measured using the isolation and Z mass spectrum fit method.

the additional track on the plug leg of CP and PP topology. With the additional track requirement, all three topologies have only two track events and the QCD background level goes down from $1.55 \pm 0.12(stat.) \pm 0.42(syst.)\%$ for CP and $3.40 \pm 0.72(stat.) \pm 0.21(syst.)\%$ for PP topology to $0.22 \pm 0.03(stat.) \pm 0.55(syst.)\%$ for CP and $0.67 \pm 0.12(stat.) \pm 0.23(syst.)\%$ for PP topology. The track requirment of both legs also removes all γ+jet background contribution (which gives more systematic uncertainty for the background estimation). Figure 3 compares the QCD background level in Z P_T for each topology.

The total number of the selected events with the orginal selection used for $d\sigma/dy$ analysis was $\sim$ 168000 events. Addiding the changes in the selection criteria, the total number of events is 138171 and the most change come from the new track requirement. The additional track requirement reduce the total events by rougly 18%, but still it covers all acceptance region in $\cos\theta$ and ϕ which could be reached by the selection used for $d\sigma/dy$ measurement [16]. Only the overall amount in each $P_{\rm T}$ bin is decreased. The $\gamma^*/Z \rightarrow ee$ MC sample is produced using CDF PYTHIA generator (with QED) and GEANT simulation of CDF detector. The calorimeter

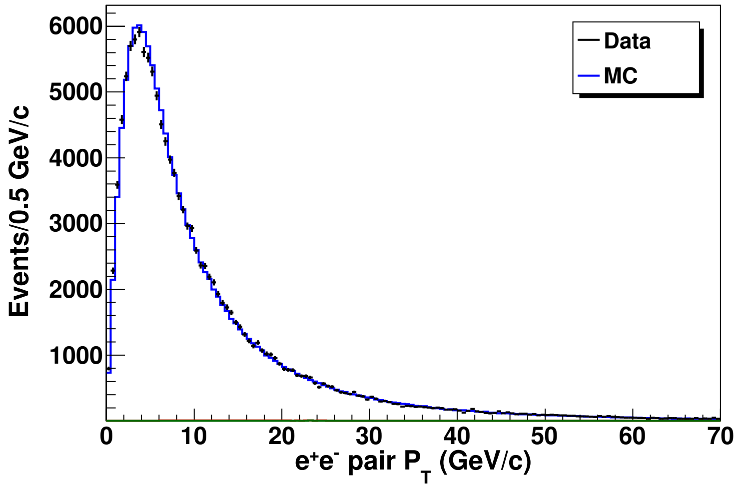

Figure 4: The P_T distribution of ee pairs of data compared to CDF PYTHIA MC. The events are selected in the mass region $66 < M_{ee} < 116$ GeV. The black crosses are data and the blue histogram is MC.

energy scale, resolutions, and selection efficiencies used in the detector simulation are tuned using data.

Figure 4 shows the comparison of γ^*/Z boson P_T distribution in data and MC. The Z P_T and y spectrum is tuned independently, for $d\sigma/dy$ measurement, so the each distribution shows a reasonable agreement between data and MC. However, Z P_T is correlated with y and this correlation is already in MC, but still need to be tuned. Therefore, we apply the Z P_T vs. y correction into MC to describe the data well. The correction factor is measured to compare the data to MC in Z P_T and y after applying all selections and subtracting the backgrounds. (This correction is the data-driven correction to avoid any model dependence effect.) Figure 5 shows the correction factor in Z P_T and y, and the Z P_T spectrum ratio of data to MC before and after the correction factor. The overall χ^2/NDF of Z P_T spectrum integrating all y between data and MC doesn't have much improvement (χ^2/NDF before correction = 1.66 and χ^2/NDF after correction = 1.51), but the correlation between two kinematics, Z P_T vs. y in MC has better matches to the data applying the correction. The χ^2/NDF of y distribution is 1.36 before the correction and 0.96 after the correction and the χ^2/NDF of the dielectron mass distribution is almost same.

After event selection, we still have the small amount of background from QCD and Electroweak processes. The QCD background is measured using the isolation extrapolation method and the mass spectrum fitting method from data directly [16] and the Electroweak background is estimated by utilizing the MC simulations. The main QCD background in this process is dijet and γ+jet process. However, the two track requirement in the event selection rejects most of γ+jet background, so only dijet background need to be considered for the QCD background. We separate W+jet background from the QCD background and consider this into one of the Electroweak

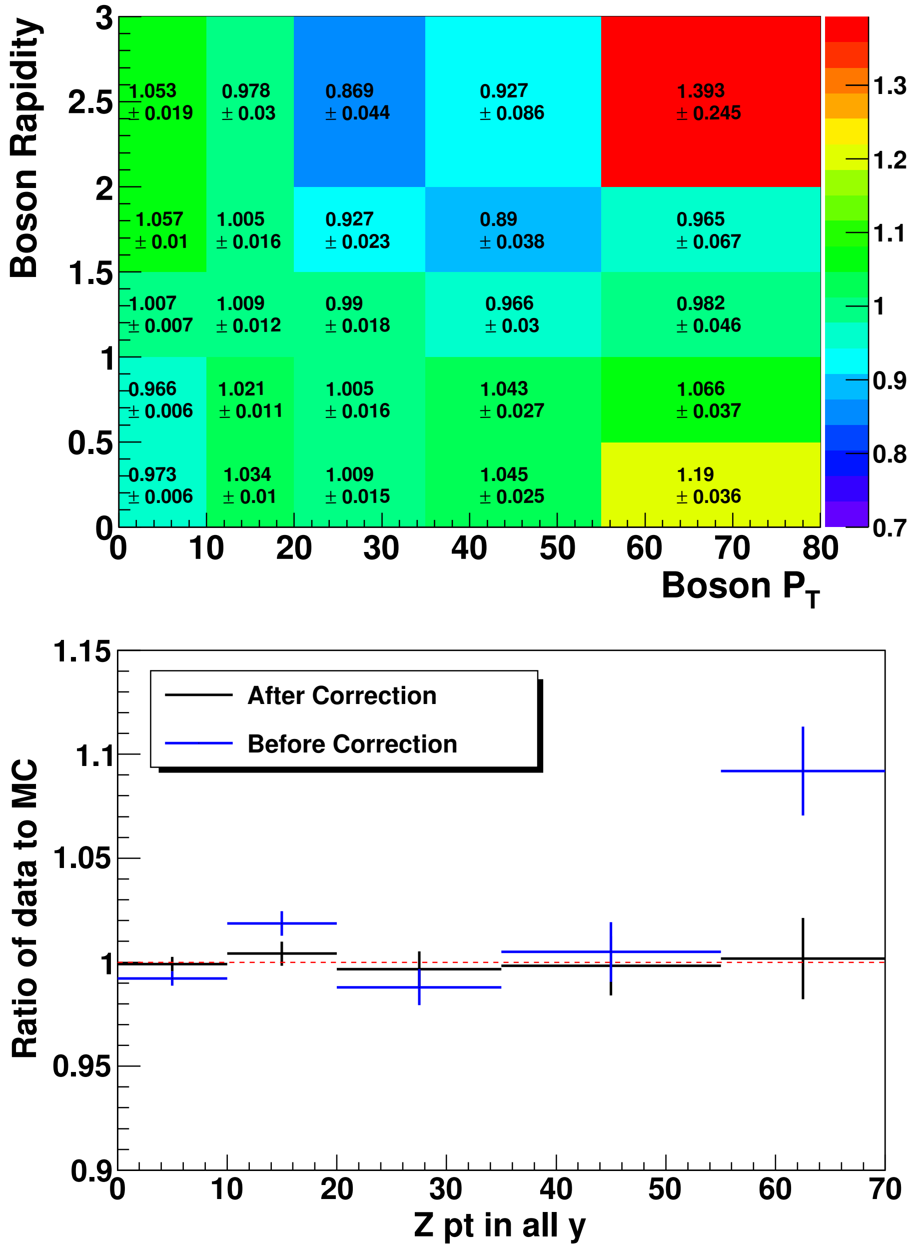

Figure 5: The top plot is the 5×5 matrix of Z P_T vs. y correction factor. The bottom plot shows the Z P_T spectrum ratio of data to MC before and after the correction factor integrating all y range. The blue crosses are the ratio of Z P_T spectrum before the correction and the black crosses are the ratio after the correction. χ^2/NDF of Z P_T spectrum before correction is 1.66 and χ^2/NDF after correction is 1.51.

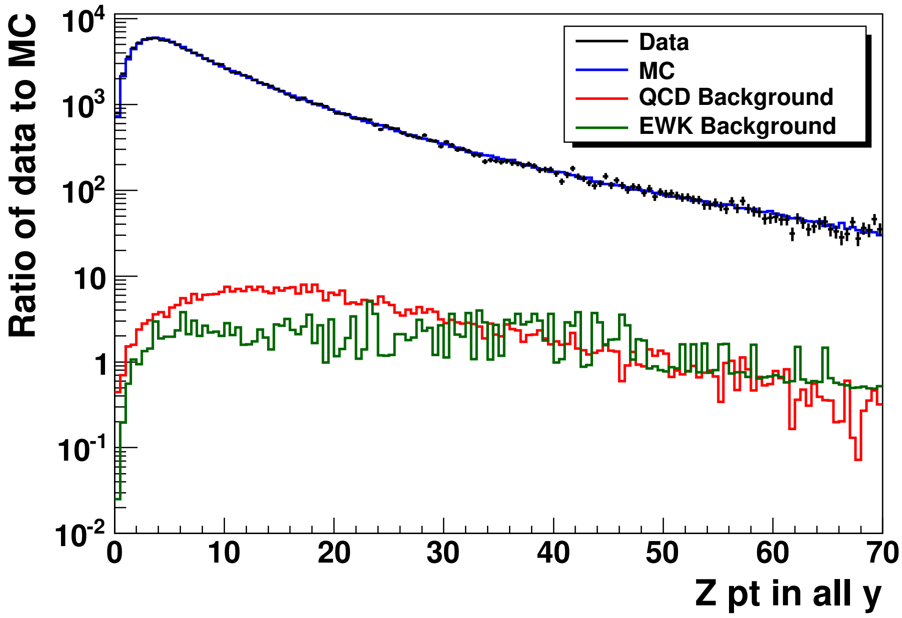

Figure 6: The P_T distribution of ee pairs of data compared to CDF PYTHIA MC. The events are selected in the mass region $66 < M_{ee} < 116$ GeV. The black crosses are data and the blue histogram is MC. The red and the green histogram corresponds to the QCD and the Electroweak background, respectively.

background processes. The total QCD background rate for CC, CP, and PP topology is 0.24±0.03%, $0.22 \pm 0.03(stat.) \pm 0.55(syst.)$%, , and $0.67 \pm 0.12(stat.) \pm 0.23(syst.)$%. To measure the background in boson P_{T}, the P_T spectrum is obtained from the background sample (data) [16] and normalized using the background fraction described above. The Electroweak background processes considered are WW, WZ, inclusive $t\bar{t}$, inclusive W+jets, and $Z \to \tau\tau$ process. We generate the MC simulations for each process and estimate the background for the corresponding the integrated luminosity. Figure 6 compares the Z P_T spectrum of data and MC and also shows the level of QCD and Electroweak background in Z P_T for CC, CP, and PP combined events. The Electroweak background is comparable to the QCD background in high P_T region ($P_{\mathrm{T}} > 40\ GeV$). The overall QCD background is 0.30% and the overall Electroweak background is 0.19%, which are very small. These remaining backgrounds are subtracted in $\cos\theta$ and ϕ for each P_{T} bin. The background distributions in $\cos\theta$ and ϕ distribution for P_{T} bin and topology are described in Appendix A - section 3.2.1.

For the efficiencies, we utilize the efficiencies measured for $d\sigma/dy$ analysis. [16] For the electron ID efficiency, we consider η and run dependence and the efficiency scale factor of data to MC is implemented into MC. For the phoenix tracking efficiency, we measured the efficiency as a function of the number of the expected silicon layers which the electron passes through (nsil) which accounts for the η and ZVertex dependence. And we also measure the efficiency in the number of vertices which accounts for the luminosity dependence. Figure 7 shows the phoenix tracking efficiency in CP

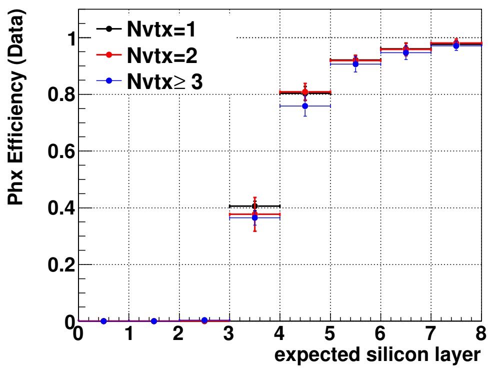

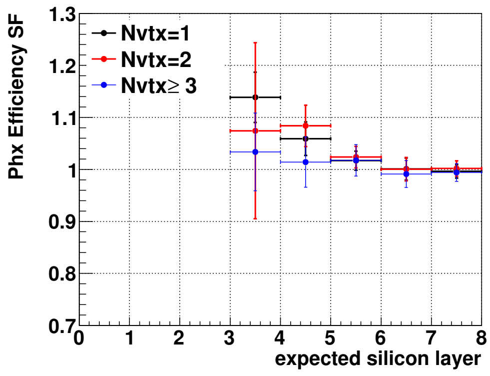

Figure 7: The plot in the left handed side shows the phoenix tracking efficiency in data for CP topology and the plot in the right handed side shows the tracking efficiency scale factor of data to MC.

topology and the scale factor of data to MC. Other efficiency values and scale factors are described in [16].

2.4 Extraction of the angular parameters in P_{T} bins

The Collins-Soper [20] CM frame lepton decay angles, $\cos\theta$ and ϕ, are:

$$\cos\theta = \frac{2}{M\sqrt{M^2 + P_{\mathrm{T}}^2}}(\ell_1^+\ell_2^- - \ell_1^-\ell_2^+) \tag{15}$$

$$\tan\phi = \frac{\sqrt{M^2 + P_{\mathrm{T}}^2}}{M} \cdot \frac{\vec{\Delta}_r \cdot \hat{R}_T}{\vec{\Delta}_r \cdot \hat{Q}_T} \tag{16}$$

where M is the mass of the dielectron pair, ℓ_1 (ℓ_2) is the four-momentum of electron (positron), P_{T} is the transverse momentum of the electron-positron pair, $\ell^{\pm}$ corresponds to $\frac{1}{\sqrt{2}}(\ell^0 \pm \ell^3)$, $\Delta^j = \ell^j - \bar{\ell}^j$, $\hat{Q_T}$ is a transverse unit vector in the direction of $\vec{Q_T}$, and $\hat{R_T}$ is a transverse unit vector in the direction of $\vec{P_A} \times \vec{Q}$.

The electron and positron of CC and CP topology dilectron pairs are accurately distinguished using the well measured track of central electrons. The CC topology only uses the oppositely charge electron pairs. For the PP topology, the plug electron tracking has significant charge misidentification so we do not distinguish the electron from the positron. Therefore, in the PP topology, we only measure $|\cos\theta|$ and ϕ (period is $-\pi/2$ to $\pi/2$) to ignore the sign of lepton, so this topology is insensitive to A_4 and A_3.

The angular distributions of the selected events is shown in Figgire 8. The events at high $|\cos\theta|$ and $\phi \sim 0$ or π ($\pi/2$ for PP topology) are rejected by the acceptance. The very high boson P_{T} is where the boost puts both leptons into the detector acceptance (see Figgure 8 - red dashed histograms corresponds to $P_{\mathrm{T}} > 35$). Especially, $\phi \sim 0$ or π region in very high boson P_{T} has one electron with very high E_T, on the other hand, another electron with very soft E_T. Therefore, the events in this region is rejected by the physics kinematic cut, E_T because of the soft electron. The overall angular distribution of the MC is in good agreement with the data. However, the angular distribution has a boson P_{T} dependence. The P_{T} dependence of the parameters in the angular distribution is determined in the following way.

First, the data and the simulated MC data are binned in the P_{T} bins, (0,10), (10,20), (20,35), (35,55), and (55 and above) using the reconstructed dielectron P_{T}. The P_{T} peak is around $P_{\mathrm{T}} \simeq 5$, so the smearing effect is large around this region. Therefore, the first bin is set to be large to minimize the smearing effect into other bins. For each P_{T} bin of the simulated data, we construct a grid of (A'_0, A'_4) points for $\cos\theta$, and (A'_2,A'_3) points for ϕ distribution about the (A_0, A_4) and (A_2, A_3) values in Table 4's $A_{0,4}^{default}$ and $A_{2,3}^{default}$. These $A_{0,4}^{default}$ and $A_{2,3}^{default}$ are PYTHIA default angular coefficients before QED radiation. The $\cos\theta$ and ϕ distributions have 50 bins for each P_{T} bins. Here, we explain the fitting procedure for $\cos\theta$ case because the fitting procedure for ϕ distribution is exactly same except for (A_2,A_3) parameter replaced by (A_0,A_4) parameter and the function used for the event weighting to tweak the input parameter.

For each grid point (A'_0, A'_4) of the P_{T} bin, we change the default (A_0, A_4) of the simulated data by reweighting each event of the simulated data with:

$$w(x) = \frac{(1+x^2) + A'_0(1-3x^2)/2 + A'_4 \cdot x}{(1+x^2) + A_0^{default}(1-3x^2)/2 + A_4^{default} \cdot x} \tag{17}$$

Here, $x = \cos\theta$ and w is the event weight. After all, the events in a P_{T} bin are reweighted to form the reweighted $\cos\theta$ distribution.

For ϕ distribution, the weighting factor is replaced by :

$$w(x) = \frac{1 + \frac{3\pi A'_3}{16}\cos\phi + \frac{A'_2}{4} \cdot \cos 2\phi}{1 + \frac{3\pi A_3^{default}}{16}\cos\phi + \frac{A_2^{default}}{4} \cdot \cos 2\phi} \tag{18}$$

The angular distibutions, $\cos\theta$ and ϕ, in the generated level are calculated in QED born level which is before QED radiation. (To calculate $\cos\theta$ and ϕ in QED born level, the four momentum of electron and positron before QED radiation is used.) Therefore, the angular coefficients, (A_0,A_4) and (A_2,A_3) used for the generated level are the coefficients before the photon radiations. The parameters used for the event weighting, ($A_0^{default}$,$A_4^{default}$) and ($A_2^{default}$,$A_3^{default}$), are PYTHIA default values without QED radiation. These values in P_{T} bins used for the measurement are described in Table 4.

The number of simulated events are normalized to that of the data to compare the shape and extract the parameters. The normalization factor (f) should be same in the generated level with any different angular coefficients modeling. because it is the luminosity factor of the sample and the angular coefficients modeling only changes the shape of the angular distributions. However, this factor after all selection cut in the reconstructed level might be changed in each topology because the acceptance and efficiency is not flat in $\cos\theta$ and ϕ distribution, so the acceptance times efficiency factor changes the event fraction of CC, CP, and PP topology. Therefore, we

P_{T}	$A_0^{default}$	$A_4^{default}$	$A_2^{default}$	$A_3^{default}$
00–10	$(.786 \pm .120)10^{-2}$	$.111 \pm .001$	$(-.254 \pm .222)10^{-2}$	$(-.460 \pm .940)10^{-3}$
10–20	$(.222 \pm .020)10^{-1}$	$.113 \pm .002$	$(.188 \pm .037)10^{-1}$	$(.093 \pm .159)10^{-2}$
20–35	$(.680 \pm .029)10^{-1}$	$.115 \pm .002$	$(.697 \pm .054)10^{-1}$	$(.228 \pm .231)10^{-2}$
35–55	$.155 \pm .005$	$.123 \pm .004$	$.178 \pm .009$	$(.441 \pm .373)10^{-2}$
> 50	$.370 \pm .007$	$.114 \pm .005$	$.368 \pm .012$	$(.126 \pm .532)10^{-2}$

Table 4: Mass region $66 < M_{ee} < 116$. Fit parameters to $\cos\theta$ and ϕ distribution for the P_{T} bins used for the measurement. PYTHIA default does not include QED initial or final state radaition.

considered the normalization factor, f, as one of fitting parameters so that the data determines the normalization factor.

To extract the angular parameters, we uses the maximum log-likelihood method using Poisson probability to take account of the data statistical fluctuations. The log-likelihood (L) of the (A_0', A_4') reweighted simulated data against the CDF Run II data is calculated in each topology varying the normalization factor, f. The log-likelihood, L, is calculated in each topology with one f value in each P_T bin, respectively, because each topology is independent sample. To combine these three topologies, we sum L of three topologies and the summed L is used to determine the best A_0 and A_4 parameter. This L calculation is done for each (A_0', A_4') grid point at certain "f" in the P_{T} bin. The resulting L's in the (A_0', A_4') grid at "f" are fit to this functional form:

$$-L(A_0', A_4') = P_0 \cdot (A_0' - A_0^0)^2 + P_1 \cdot (A_4' - A_4^0)^2 + P_2 \times (A_0' - A_0^0)(A_4' - A_4^0) + L_0 \quad (19)$$

The fit parameters are the inverse error matrix terms P_0, P_1, P_2, the minimum -L in the grid is L_0, and the angular coefficients correspoinding to the minimum -L on the grid is (A_0^0, A_4^0). Varying the normalization factor, "f", the minimum L_0 and (A_0^0,A_4^0) combination is determined as a function of f, which is L_0(f), A_0^0(f), and A_4^0(f). The normalization factor which gives the smallest L_0, f^0, is determined by fitting L_0(f) and the (A_0^0,A_4^0) combination corresponding to f^0 is assigned as the extracted angular coefficients from the data. The plots showing the correlation between the angular coefficients vs. the normalization factor are posted in Appendix A - section 3.2.2. Figure 20, 21, and 22 show L_0, A_0, and A_4 in f from $\cos\theta$ fitting and Figure 23, 24, and 25 show L_0, A_2, and A_3 in f from ϕ fitting.

The error of A_0 and A_4 is determined from the inverse error matrix, V^{-1}:

$$V^{-1} = \begin{pmatrix} \frac{\partial^2\chi^2}{\partial^2 A_0'} & \frac{\partial^2\chi^2}{\partial A_4' \partial A_0'} \\ \frac{\partial^2\chi^2}{\partial A_0' \partial A_4'} & \frac{\partial^2\chi^2}{\partial^2 A_4'} \end{pmatrix} = \begin{pmatrix} 2 \cdot P_0 & P_2 \\ P_2 & 2 \cdot P_1 \end{pmatrix} \quad (20)$$

where P_0, P_1, and P_2 are the parameters from the fit to the grid points in L. The errors in the extracted values of A_0 and A_4 are from the error matrix components, $\sqrt{V_{11}}$ and $\sqrt{V_{22}}$. These calculated errores of A_0 and A_4 are flat in the normalization factor, f. The normalization factor from the fitter in P_{T} bin is relatively flat which is shown in Figure 9.

(a) $\cos\theta$ and ϕ in CC topology

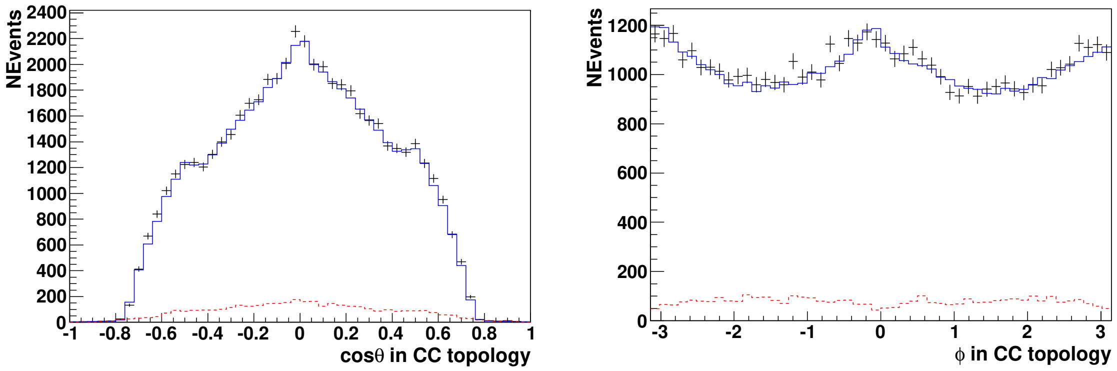

(b) $\cos\theta$ and ϕ in CP topology

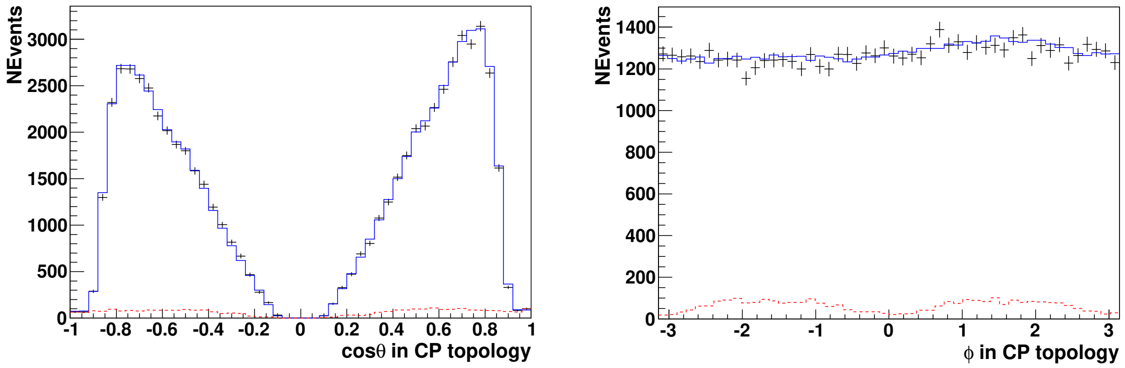

(c) $\cos\theta$ and ϕ in PP topology

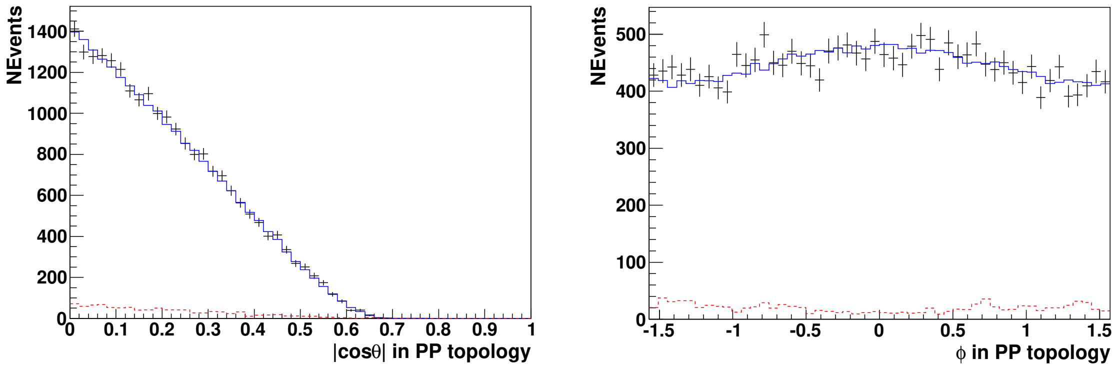

Figure 8: The angular distributions, $\cos\theta$ and ϕ, for each topology. The black crosses are the data and the blue histograms are PYTHIA MC integrating all P_{T}. The red dashed histograms are the data for $P_{\mathrm{T}} > 35\ GeV$ region.

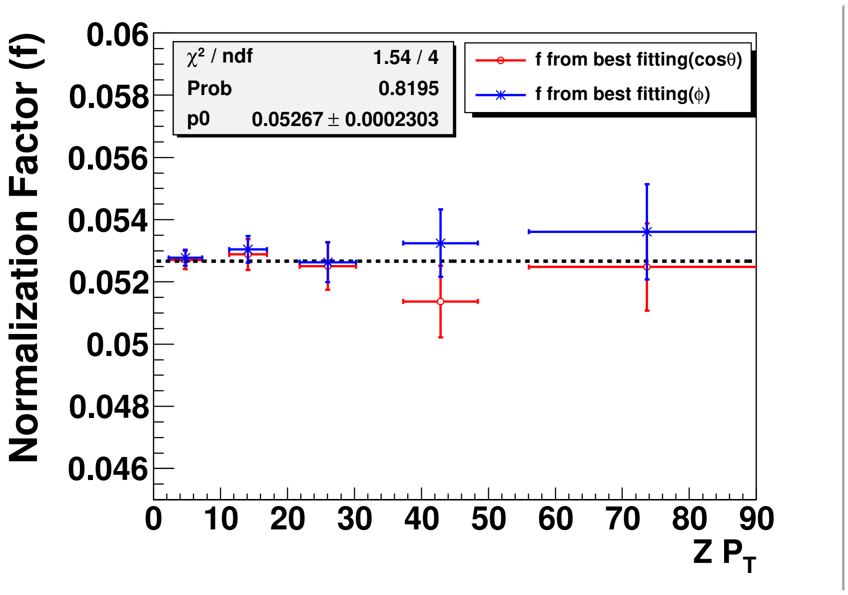

Figure 9: The normalization factor of data to MC in Z P_{T}. The red points are the normalization factor from $\cos\theta$ fitting and the blue points are the normalization factor from ϕ fitting. The normalization factors are consistent within one deviation of error.

2.4.1 Correlation of $\cos\theta$ and ϕ

The angular distributions, $\cos\theta$ and ϕ, are independent each other in the generated level. However, the reconstructed $\cos\theta$ and ϕ distribution has the correlation each other because of the acceptance and efficiency effect. To minimize this effect, we iterate the fitting procedure. First, we start with the angular parameters of PYTHIA default and tweak (A_0,A_4) in the generated level for $\cos\theta$ fitting or (A_2,A_3) for ϕ fitting. (This procedure is already performed in section 2.4.) This extracted angular parameters are implemented into MC generated level. And then, the fitting procedure is repeated to extract the angular parameters. This procedure is repeated until the extracted angular parameters are converged. In each step, the extracted angular parameters in the previous step are implemented in the generated level of MC simulations. From the iteration procedure, we find that the central values of A_0 and A_2 in the high P_{T} bin, (35,55) and (55 and above), are slightly shift. The angular coefficients in the low P_{T} region are same in each iteration step and also A_3 and A_4 coefficients are not changed, either. Figure 10, and 11 show the iteration result of the angular parameters in high P_{T} bins, (35,55) and (55 and above).

2.5 Goodness of Fit

To test the goodness of fit, we calculate χ^2 of the data and the prediction which is modified by the extracted angular coefficients from the data. (This modified prediction has the best matching with the data.) Table 5 describes χ^2 for each topology and P_{T} bin. The χ^2/NDF is calculated for (CC+CP+PP) all combined topology.

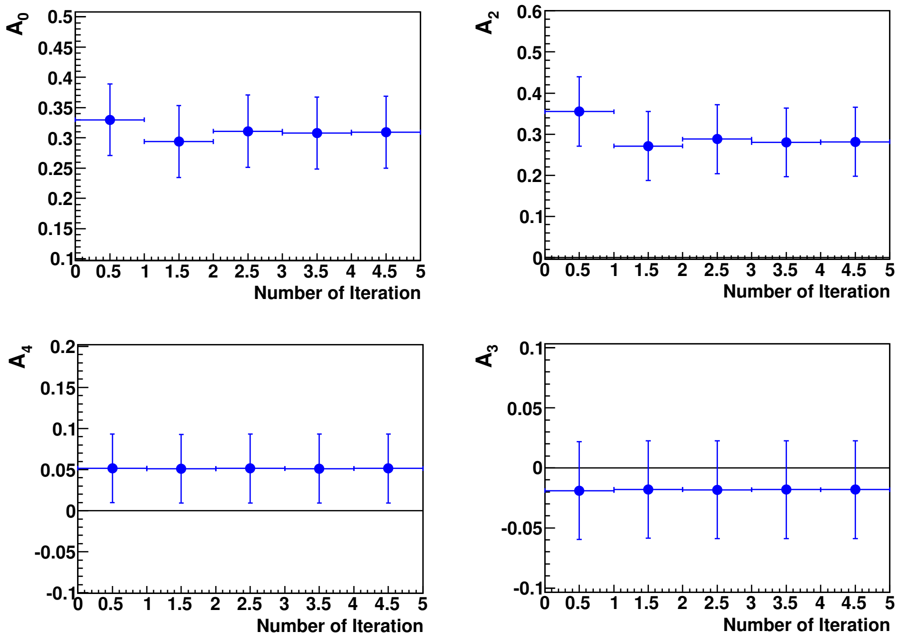

Figure 10: The extracted angular parameters in each iteration for Z P_{T} bin, (35,55).

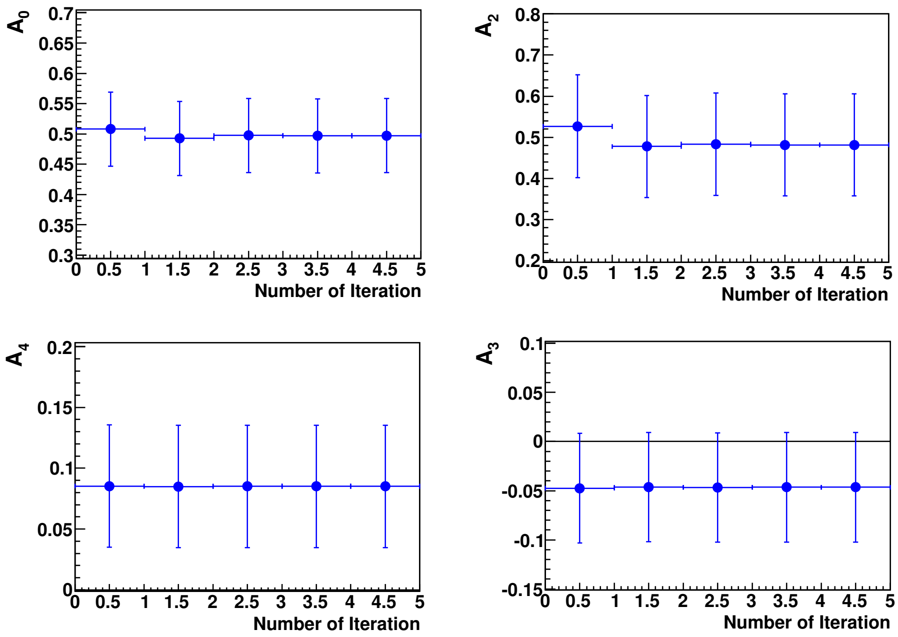

Figure 11: The extracted angular parameters in each iteration for Z P_{T} bin, (55 and above).

(a) χ^2 from $\cos\theta$ distribution

P_{T} bins	χ^2 (CC)	χ^2 (CP)	χ^2 (PP)	χ^2 (All)	NDF	χ^2/NDF
00–10	52.7	40.0	29.5	122.2	115	1.06
10–20	42.1	39.6	25.4	107.2	117	0.92
20–35	31.7	52.8	42.1	126.5	119	1.06
35–55	61.0	79.9	45.1	186.0	125	1.49
> 55	72.3	58.0	45.0	175.3	138	1.27

(b) χ^2 from ϕ distribution

P_{T} bins	χ^2 (CC)	χ^2 (CP)	χ^2 (PP)	χ^2 (All)	NDF	χ^2/NDF
00–10	34.9	56.0	54.8	145.7	147	0.99
10–20	68.8	48.9	43.8	161.5	147	1.10
20–35	61.2	33.5	55.4	150.0	147	1.02
35–55	66.0	35.0	53.7	154.6	147	1.05
> 55	75.6	44.8	58.9	179.2	147	1.22

Table 5: χ^2 summaries for the topologies and P_{T} bins. χ^2/NDF for all P_{T} bins are close to 1.0 which shows a good agreement.

The χ^2/NDF for P_{T} regions are closed to be 1.0 which implies that the fitting quality is good. For the cross check of fitting quality, we also plot $\cos\theta$ and ϕ distribution in P_{T} bin and check the ratio of the data to MC (with the best matching points or with the default PYTHIA angular coefficients). The plots are posted in Appendix A - section 3.2.3.

2.6 Systematic Uncertainties

The systematic uncertainties which were considered in the $d\sigma/dy$ measurement [16] are checked for this angular coefficients measurement. The biggest uncertainty source of the $d\sigma/dy$ analysis is the luminosity factor ($\sim 6\%$). This luminosity factor is the global factor, so only affects on the normalization of events. We apply 6% change into the selected signal yield and then extract the angular parameters. However, the extracted angular coefficients are exactly same between with and without 6% change. Therefore, we ignore the systematic uncertainty for the luminosity factor.

The QCD background in the sample is $\sim 0.30\%$ level and the Electroweak background in the sample is $\sim 0.19\%$ in total. The $\cos\theta$ shape of the background events are close to the signal shape, so A_0 and A_4 parameters don't affect much from the background. However, the ϕ shape of background events are different, so A_2 and A_3 parameters are more sensitive to the background. To assign the systematic uncertainty for the background, we extract the angular parameters with and without the background subtraction. The difference of the angular parameters extracted with and without the background subtraction is assigned as a systematic uncertainty for the background estimation. This systematic uncertainty for the background estimation is the biggest systematic uncertainty source in the measurement.

The material modeling in the detector affects on the acceptance. For estimating the material modeling effect in the measurement, we use three PYTHIA simulation data sets (each sample include the different material input). The first sample includes the default material input which is CDF default input for the official PYTHIA MC. The second sample includes more extra material in the central calorimeter by 1% and the third sample includes more material in the plug calorimeter by $\frac{1}{6}X_0$. The central and plug calorimeters are independent component of the detector each other. Therefore, we estimate the material modeling effect for the central and plug calorimeter, respectively, comparing the extra material sample in the central calorimeter (second sample) with the default sample (first sample) or the extra material sample in the plug calorimeter (third sample) with the default sample (first sample). At the end, The systematic uncertainty for the material modeling is assigned by summing up the uncertainties from the central region and plug region in quadrature.

The Z P_{T} vs. rapidity(y) correction is applied into MC to tune PYTHIA modeling for Z P_T and rapidity. This correction is the data-driven factor, so the most uncertainty comes from the statistics of the data. We vary the statistical uncertainty of the correction factor by 1 σ deviation and estimate the deviations in the angular distributions. The deviation in the extracted angular parameters varying the correction factor is assigned as a systematic uncertainty.

The electron identification (ID) and the phoenix tracking efficiencies are measured using the data. To match MC to data, the efficiency scale factors of data to MC are applied into MC. For the systematic uncertainty of ID and phoenix tracking efficiency, we vary the efficiency scale factors with 1 σ change. The difference from the scale factor changes is assigned as a systematic uncertainty for the efficiency factors.

The electron energy scale is applied into MC in order to make a good agreement between data and MC. The energy scale is applied in η. We shift the energy scale by 1 σ deviation in η and estimate the difference in the measured angular distributions for the systematic uncertainty.

There is no correlation among the sources of the systematic uncertainty, so the uncertainties are summed in quadrature for the total systematic uncertainty. The total systematic uncertainty is small compared to the statistical uncertainty which is shown in Figure 12.

2.7 Result

We measure the angular coefficients, A_0, A_2, A_3, and A_4 in the mass region, $66 < M_{ee} < 116$ GeV for each Z P_{T} bin. The measured angular coefficients correspond to the coefficients before QED radiation (QED born level). Figure 13 and 14 show the measured angular coefficients in Z P_{T}. We compare the measurement to the various predictions which are PYTHIA, PYTHIA+1jet, QCD calculations in the fixed order perturbation theory (DYRAD, MADGRAPH, POWHEG, and FEWZ), and QCD calculations with resummation (RESBOS and VBP). The PYTHIA and VBP predictions are close in P_{T} and follow the approximation of $q\bar{q}$ annihilation process, $\frac{P_T^2}{P_T^2+M_{\ell\ell}^2}$.

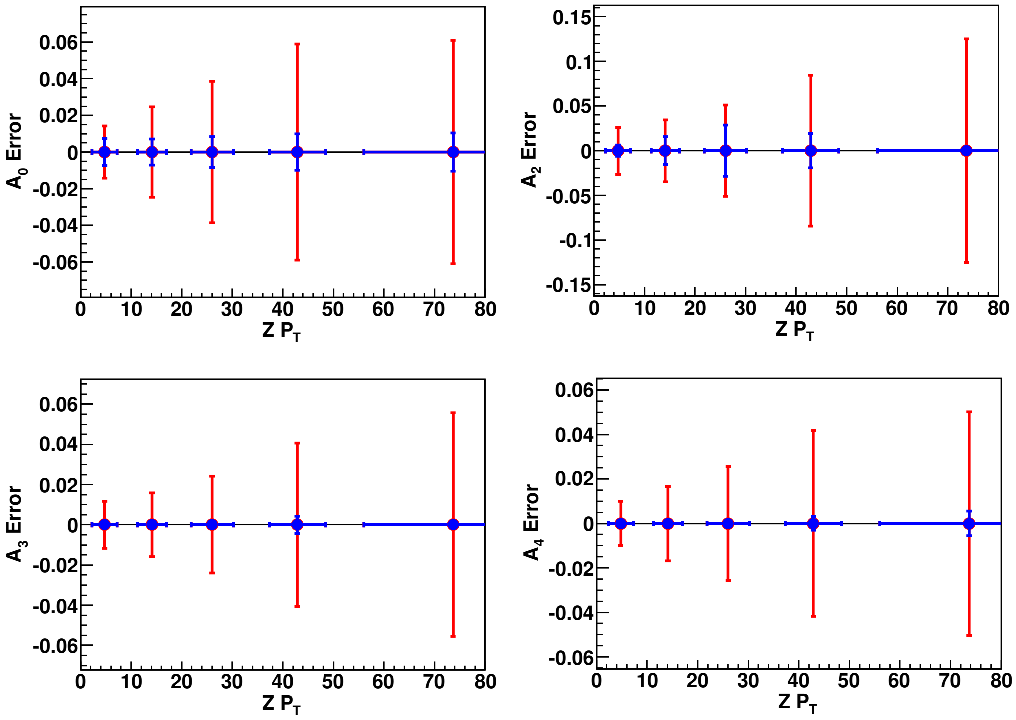

Figure 12: The systematic uncertainty vs. the statistical uncertainty for the angular parameters. The red and blue bars correspond to the statistical and systematic uncertainty, respectively. The statistical uncertainty is dominant in the measurement.

Other higher order predictions like DYRAD, MADGRAPH, POWHEG, FEWZ, and PYTHIA+1jet are close and have the higher A_0 and A_2 values than PYTHIA in high Z P_{T} region. The RESBOS prediction follows PYTHIA in low P_{T} region, but cross over to the high order predictions in $P_{\mathrm{T}} > 35$ GeV.

A_0 and A_2 have a strong P_{T} dependence. The measured A_0 and A_2 follows PYTHIA prediction in low P_{T} bin, up to $P_{\mathrm{T}} < 35$, but prefer the high order predictions (DYRAD, MADGRAPH, POWHEG, FEWZ, and PYTHIA+1jet) in $P_{\mathrm{T}} > 35$. In $P_{\mathrm{T}} > 35$ region, the measured A_0 is higher than PYTHIA prediction by roughly 1.5 to 2σ and the measured A_2 is higher within 1σ uncertainty. In addition, we confirm the Lam-Tung relation ($A_0 \simeq A_2$) which is only valid for vector gluon theory. The average of $A_0 - A_2$ is measured to be 0.017 ± 0.023, which is consistent with zero within the uncertainty. $A_0 - A_2$ for all P_{T} bins are also consistent with zero within 1 σ deviation of the uncertainty , which is summarized in Table 13. The measured A_0 and A_2 in boson P_{T} are shown in Figure 13.

The A_3 and A_4 parameters are relatively flat in Z P_{T}. The central value of A_3 parameter is slightly going down in P_{T}, but consistent with zero within one deviation of the uncertainty. The A_4 parameter determines the forward and backward asymmetry of Drell-Yan process which has a mass dependence. Here, we measure A_4 integrating of the mass range, $66 < M_{ee} < 116GeV/c^2$. The A_4 parameter is sensitive to Weinberg angle, $\sin\theta_W^2$. To compare the measured A_4 with the predictions, we generate the predictions fixing $\sin\theta_W^2 = 0.232$. The predictions are closed around $A_4 \sim 0.12$ and the measured A_4 is consistent with predictions within 1.5 σ deviation of the uncertainty. The measured A_3 and A_4 in boson P_{T} are shown in Figure 14.

The measured angular coefficients and PYTHIA predictions in P_{T} are summarized in Table 6 and 7.

The angular coefficients, A_0, A_2, A_3, and A_4, are measured in boson P_{T} and these coefficients agree with PYTHIA prediction except A_0 and A_2 in high P_{T} region. Even in high P_{T} region, the deviation between the measurement and PYTHIA prediction is 1.0 to 2.0 σ level difference which is not large. In addition, the event fraction of $P_{\mathrm{T}} > 35$ GeV region to total is less than 6%. Therefore, PYTHIA MC has a good agreement with the data for the overall angular distributions integrating P_{T}. And this results that the acceptance effect on $d\sigma/dy$ measurement [16] for the angular distribution modeling (which is the first motivation of this study) is negligible.

2.8 Conclusion

We measure the angular coefficients, A_0, A_2, A_3, and A_4 in Z P_{T}. The angular coefficients which have a strong P_{T} dependence, A_0 and A_2 agree with PYTHIA in low P_{T} region, $P_{\mathrm{T}} < 35$ GeV. In high P_{T} region , the measured A_0 and A_2 have better agreements with the higher order QCD predictions (DYRAD, MADGRAPH, POWHEG, FEWZ, and PYTHIA+1jet). The A_3 and A_4 parameters agree with PYTHIA, VBP, and RESBOS predictions within the uncertainty. We also conclude that PYTHIA MC simulates the data in a reasonbale level for the angular distributions (The deviation is only shown in A_0 parameter in high P_{T} region up to by 2σ uncertainty) , so the angular distribution modeling in PYTHIA MC doesn't affect on the acceptance of

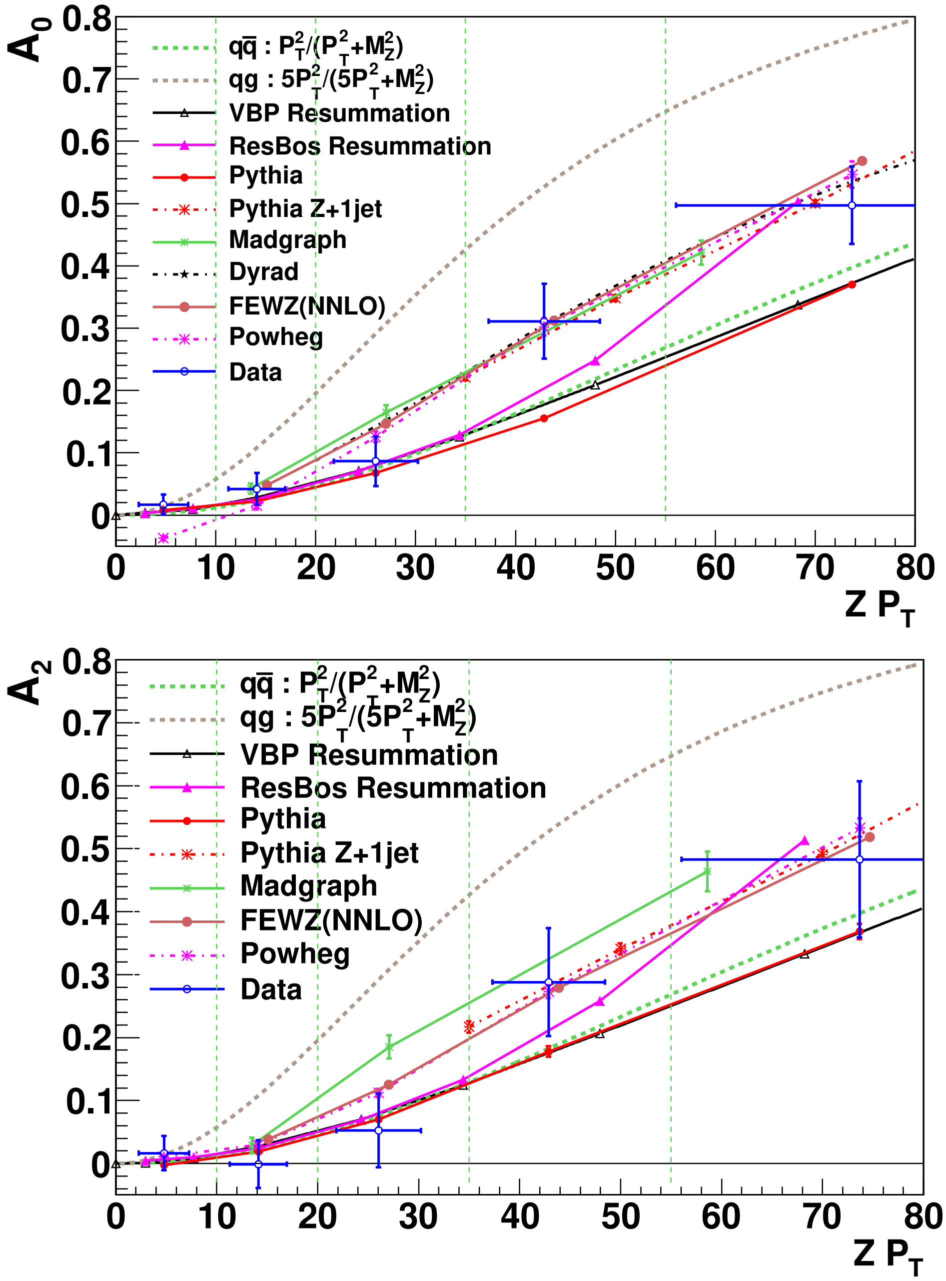

Figure 13: The measured A_0 and A_2 and predictions in P_{T} for the mass window, $66 < M_{ee} < 116\ GeV/c^2$. A_0 and A_2 have a strong P_{T} dependence. the Lam-Tung relation ($A_0 \simeq A_2$) which is only valid for vector gluon theory is confirmed. (The average of $A_0 - A_2$ is measured to be 0.017 ± 0.023.) For the measured A_0 and A_2, the uncertainties correspoind to the total uncertainties ($stat. \oplus syst.$)

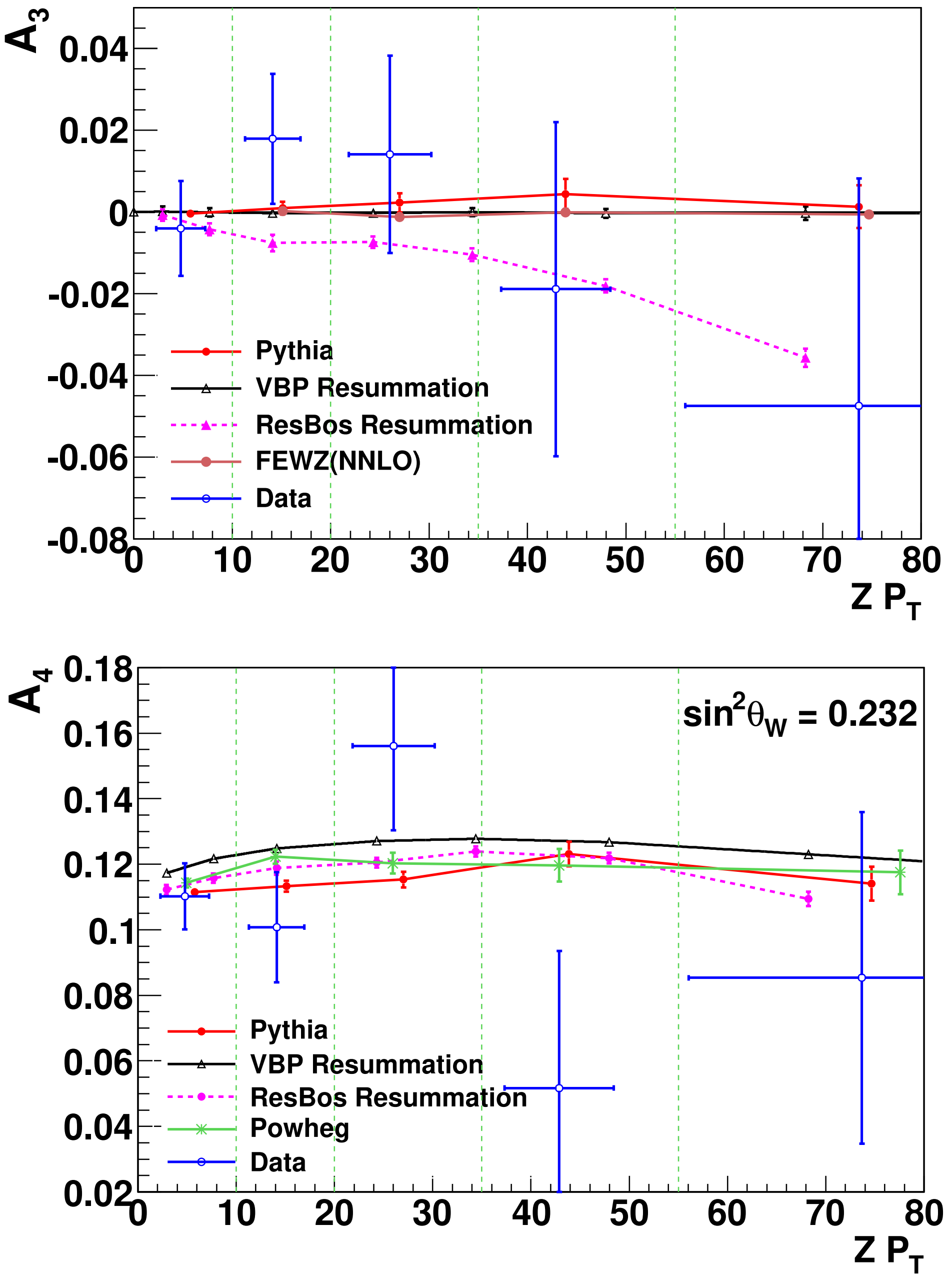

Figure 14: The measured A_3 and A_4 and predictions in P_{T} for the mass window, $66 < M_{ee} < 116\ GeV/c^2$. A_3 and A_4 are relatively flat in P_{T}. For the measured A_3 and A_4, the uncertainties correspoind to the total uncertainties ($stat. \oplus syst.$)

	CDF PYTHIA Prediction	
P_{T} bin (GeV)	A_0	A_4
00–10 (4.8)	$(.782 \pm .120)10^{-2}$	$.111 \pm .001$
10–20 (14.1)	$(.221 \pm .020)10^{-1}$	$.113 \pm .002$
20–35 (26.0)	$(.680 \pm .029)10^{-1}$	$.115 \pm .002$
35–55 (42.9)	$.155 \pm .005$	$.123 \pm .004$
> 55 (73.7)	$.370 \pm .007$	$.114 \pm .005$

	Data	
P_{T} bin (GeV)	A_0 CDF	A_4 CDF
00–10 (4.8)	$(.170 \pm .142^{(stat.)} \pm .073^{(syst.)})10^{-1}$	$.110 \pm .010 \pm .001$
10–20 (14.1)	$(.422 \pm .245 \pm .071)10^{-1}$	$.101 \pm .017 \pm .001$
20–35 (26.0)	$(.865 \pm .387 \pm .085)10^{-1}$	$.156 \pm .026 \pm .001$
35–55 (42.9)	$.311 \pm .059 \pm .010$	$.052 \pm .042 \pm .003$
> 55 (73.7)	$.497 \pm .061 \pm .010$	$.085 \pm .050 \pm .005$

Table 6: Fit parameters (A_0,A_4) to CDF PYTHIA prediction and data in boson P_{T} for the mass window, $66 < M_{ee} < 116 GeV/c^2$. The parameters, A_0 and A_4, are measured by fitting $\cos\theta$ distribution. The CDF PYTHIA prediction before QED radiation (CDF MC). In the "P_{T} bin" column, the number in parenthesis is the mean P_{T} in the bin.

	CDF PYTHIA Prediction	
P_{T} bin (GeV)	A_2	A_3
00–10 (4.8)	$(-.255 \pm .222)10^{-2}$	$(-.435 \pm .940)10^{-3}$
10–20 (14.1)	$(.187 \pm .037)10^{-1}$	$(.093 \pm .159)10^{-2}$
20–35 (26.0)	$(.697 \pm .054)10^{-1}$	$(.226 \pm .231)10^{-2}$
35–55 (42.9)	$.178 \pm .009$	$(.439 \pm .371)10^{-2}$
> 55 (73.7)	$.368 \pm .012$	$(.129 \pm .523)10^{-2}$

	Data	
P_{T} bin (GeV)	A_2 CDF	A_3 CDF
00–10 (4.8)	$(.165 \pm .263^{(stat.)} \pm .061^{(syst.)})10^{-1}$	$(-.041 \pm .116 \pm .006)10^{-1}$
10–20 (14.1)	$(-.012 \pm .347 \pm .155)10^{-1}$	$(.179 \pm .159 \pm .002)10^{-1}$
20–35 (26.0)	$(.524 \pm .511 \pm .286)10^{-1}$	$(.141 \pm .241 \pm .013)10^{-1}$
35–55 (42.9)	$.288 \pm .084 \pm .019$	$(-.189 \pm .407 \pm .043)10^{-1}$
> 55 (73.7)	$.483 \pm .124 \pm .002$	$(-.474 \pm .556 \pm .020)10^{-1}$

Table 7: Fit parameters (A_2,A_3) to CDF PYTHIA prediction and data in boson P_{T} for the mass window, $66 < M_{ee} < 116 GeV/c^2$. The parameters, A_2 and A_3, are measured by fitting ϕ distribution. The CDF PYTHIA prediction before QED radiation (CDF MC). In the "P_{T} bin" column, the number in parenthesis is the mean P_{T} in the bin.

Data for Lam-Tung Relation	
$P_{\rm T}$ bin (GeV)	$A_0 - A_2$
00–10 (4.8)	$(.005 \pm .314)10^{-1}$
10–20 (14.1)	$(.434 \pm .458)10^{-1}$
20–35 (26.0)	$(.341 \pm .706)10^{-1}$
35–55 (42.9)	$.023 \pm .105$
> 55 (73.7)	$.014 \pm .139$

Table 8: The measured Lam-Tung relation ($A_0 \simeq A_2$) in Z $P_{\rm T}$ for the mass window, $66 < M_{ee} < 116 GeV/c^2$. The Lam-Tung relation is only valid for vector gluon theory. The uncertainties shown in this table correspond to the total uncertainty ($stat. \bigoplus syst.$).

$d\sigma/dy$ measurement [16].

3 Appendix A - The data measurements

3.1 Angular parameters in $85 < M_{ee} < 95$ GeV/c^2

The photon radiation increases at low boson mass. In addition, because the asymmetry chages sign from high to low mass, the effect of finite P_T mostly cancel out between low and high mass. To get the angular parameters for only Z bosons, we apply the tight mass window, $85 < M_{ee} < 95$ GeV/c^2, and extract the angular parameters, A_0, A_2, A_3, and A_4, from data using the same techinique described in Section 2.3. The extracted parameters are determined as a function of boson $P_{\rm T}$. Table 9 and 10 summarizes the extracted (A_0,A_4) and (A_2,A_3) from the data and compares the measurement with PYTHIA prediction. For the PYTHIA predictions, the A_0, A_2, and A_3 parameters do not change in the mass range, but A_4 shows up to $\sim 25\%$ increase in low $P_{\rm T}$ compared to the mass range of 66 to 116 GeV/c^2. The expected dependence of A_0 and A_2 on P_T is now clearly seen in the measurement. Figure 15 and 16 show the extracted angular coefficients from data in boson $P_{\rm T}$ with the mass range of $85 < M_{ee} < 95$ GeV/c^2 and compare the measurement in tight mass window with the wider mass window, $66 < M_{ee} < 116$ GeV/c^2. In the tight mass window, the background level is very small (the full Z boson mass window, $66 < M_{ee} < 116$ GeV/c^2 is already very small which is less than 0.4% level (QCD and Electroweak combined background) in total). Therefore, we ignore the background subtraction in the tight mass window, $85 < M_{ee} < 95$ GeV/c^2 because we expect the background level in the tighter mass window is smaller than the full Z boson mass window. In addition, the iteration procedure to minimize the correlation between $\cos\theta$ and ϕ distribution is skipped here. Therefore, the central value for A_0 and A_2 in the high $P_{\rm T}$ region might be shift (affected) a little bit if we consider the iteration procedure in the tight mass region. To compare the result with two different mass window in the same condition, we present the measured angular coefficients with the

	CDF PYTHIA Prediction	
P_{T} bin (GeV)	A_0	A_4
00–10 (4.8)	$(.790 \pm .131)10^{-2}$	$.136 \pm .001$
10–20 (14.1)	$(.229 \pm .022)10^{-1}$	$.131 \pm .002$
20–35 (26.0)	$(.696 \pm .032)10^{-1}$	$.128 \pm .003$
35–55 (42.9)	$.151 \pm .005$	$.126 \pm .004$
> 55 (73.7)	$.373 \pm .007$	$.108 \pm .006$

	Data	
P_{T} bin (GeV)	A_0 CDF	A_4 CDF
00–10 (4.8)	$(.172 \pm .161(stat.))10^{-1}$	$.130 \pm .011$
10–20 (14.1)	$(.629 \pm .283)10^{-1}$	$.122 \pm .019$
20–35 (26.0)	$(.754 \pm .443)10^{-1}$	$.183 \pm .029$
35–55 (42.9)	$.343 \pm .068$	$.010 \pm .047$
> 55 (73.7)	$.564 \pm .068$	$.087 \pm .056$

Table 9: Fit parameters (A_0,A_4) to CDF PYTHIA prediction and data in boson P_{T} for the tight mass window, $85 < M_{ee} < 95 GeV/c^2$ mass window. The parameters, A_0 and A_4, are measured by fitting $\cos\theta$ distribution. The CDF PYTHIA prediction before QED radiation (CDF MC). In the "P_{T} bin" column, the number in parenthesis is the mean P_{T} in the bin. The statistical uncertainty is only considered.

mass window, $66 < M_{ee} < 116$ GeV/c^2 skipping the iteration procedure which considers $\cos\theta$ and ϕ correlation in Figure 15 and 16. As shown in Figure 15 and 16, the mass dependence for the angular coefficients is not strong except A_4 parameter.

3.2 Additional plots for the measurement

3.2.1 Background in $\cos\theta$ and ϕ

We measure the background in $\cos\theta$ and ϕ distribution and the measured background is subtracted to extract the angular coefficients. In this section, the plots of background distribution in $\cos\theta$ and ϕ are posted for each topology and P_{T} bin. Figure 17, 18, and 19 corresponds to the CC, CP, and PP topology, respectively.

3.2.2 Correlation between the angular coefficients vs. f

As we describes in section 2.4, the correlation between the angular coefficients and the normalization factor of data to MC, f, is considered in the fitter to extract the angular coefficients. The plots showing the correlations are posted in this section. The $\cos\theta$ and ϕ fittings are independent procedure, one set of plots are from $\cos\theta$ fitting and another set of plots are from ϕ fitting. Figure 20, 21, and 22 show L_0, A_0, and A_4 in f from $\cos\theta$ fitting and Figure 23, 24, and 25 show L_0, A_2, and A_3 in f from ϕ fitting.

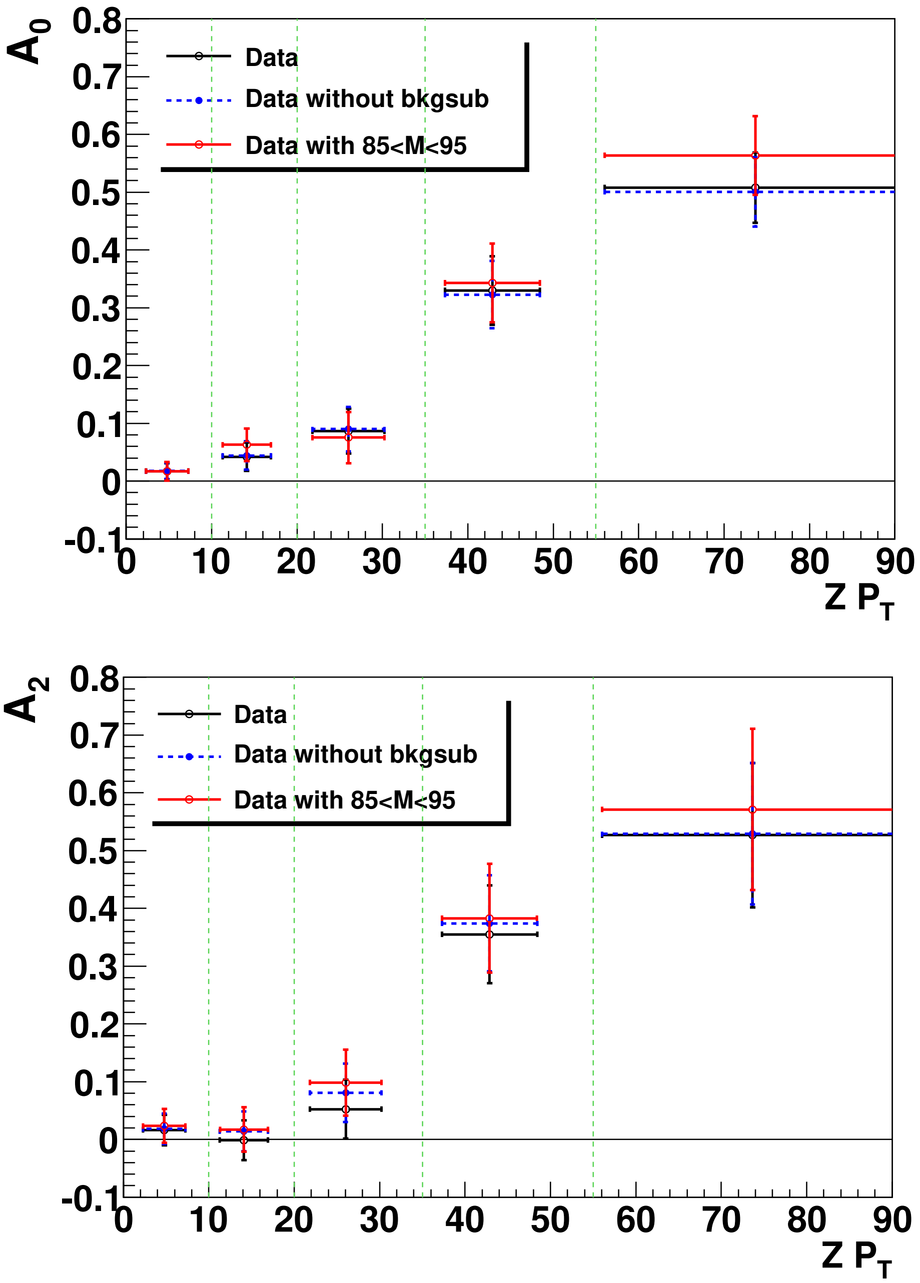

Figure 15: The measured A_0 and A_2 and predictions in $P_{\rm T}$ for the mass windows, $66 < M_{ee} < 116\ GeV/c^2$ and $85 < M_{ee} < 95\ GeV/c^2$. A_0 and A_2 have a strong $P_{\rm T}$ dependence. The measured angular coefficients are before the iteration which considers the correlation between $\cos\theta$ and ϕ. The black points are the measured angular coefficients for $66 < M_{ee} < 116\ GeV/c^2$ mass window, the blue points are the measurement for $66 < M_{ee} < 116\ GeV/c^2$ mass window without the background subtraction, and the red points are the measurement for the tight mass window, $85 < M_{ee} < 95\ GeV/c^2$. The statistical uncertainty is only considered.

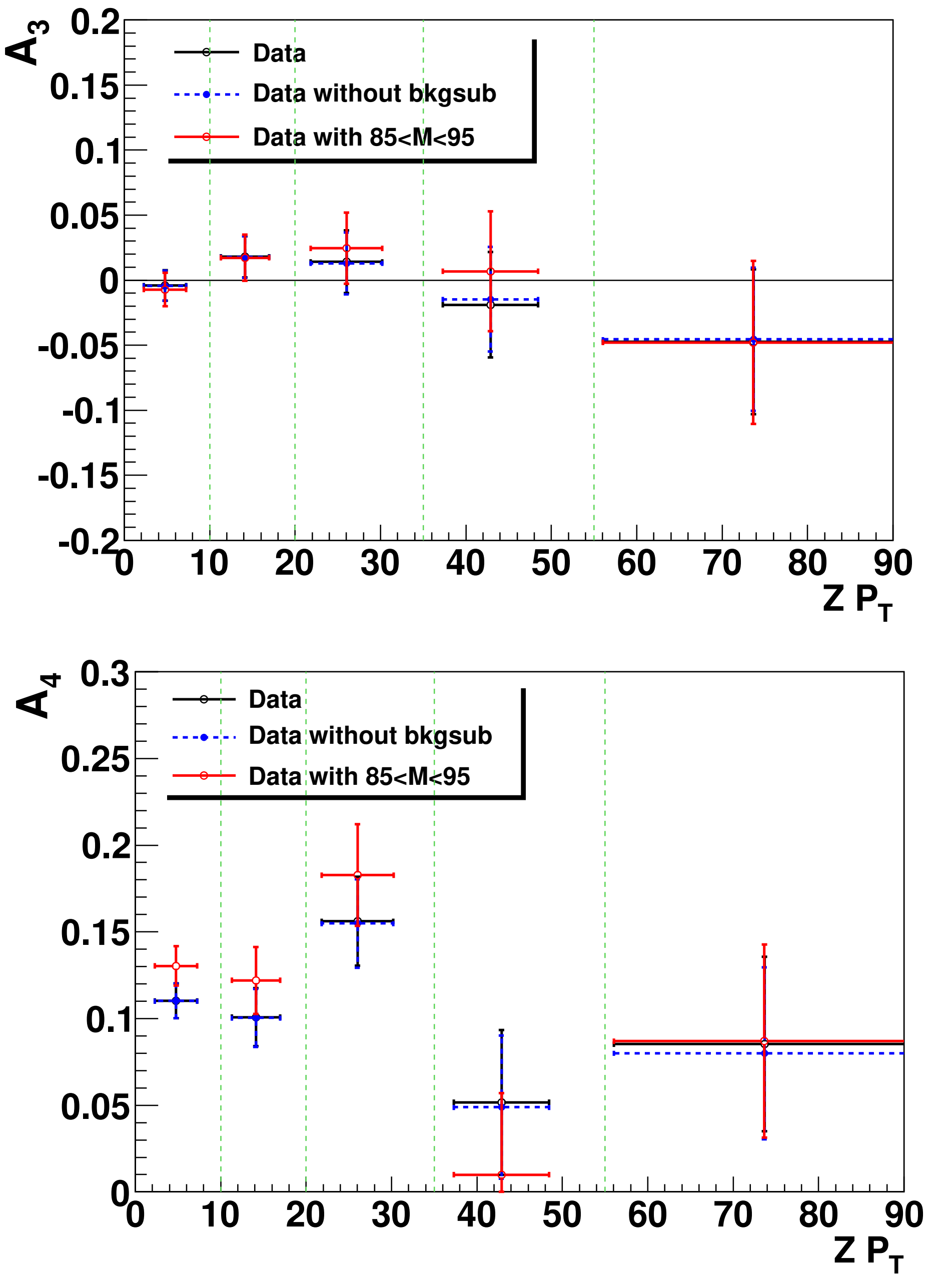

Figure 16: The measured A_3 and A_4 and predictions in P_{T} for the mass windows, $66 < M_{ee} < 116\ GeV/c^2$ and $85 < M_{ee} < 95\ GeV/c^2$. A_3 and A_4 are relatively flat in P_{T}. The measured angular coefficients are before the iteration which considers the correlation between $\cos\theta$ and ϕ. The black points are the measured angular coefficients for $66 < M_{ee} < 116\ GeV/c^2$ mass window, the blue points are the measurement for $66 < M_{ee} < 116\ GeV/c^2$ mass window without the background subtraction, and the red points are the measurement for the tight mass window, $85 < M_{ee} < 95\ GeV/c^2$. The statistical uncertainty is only considered.

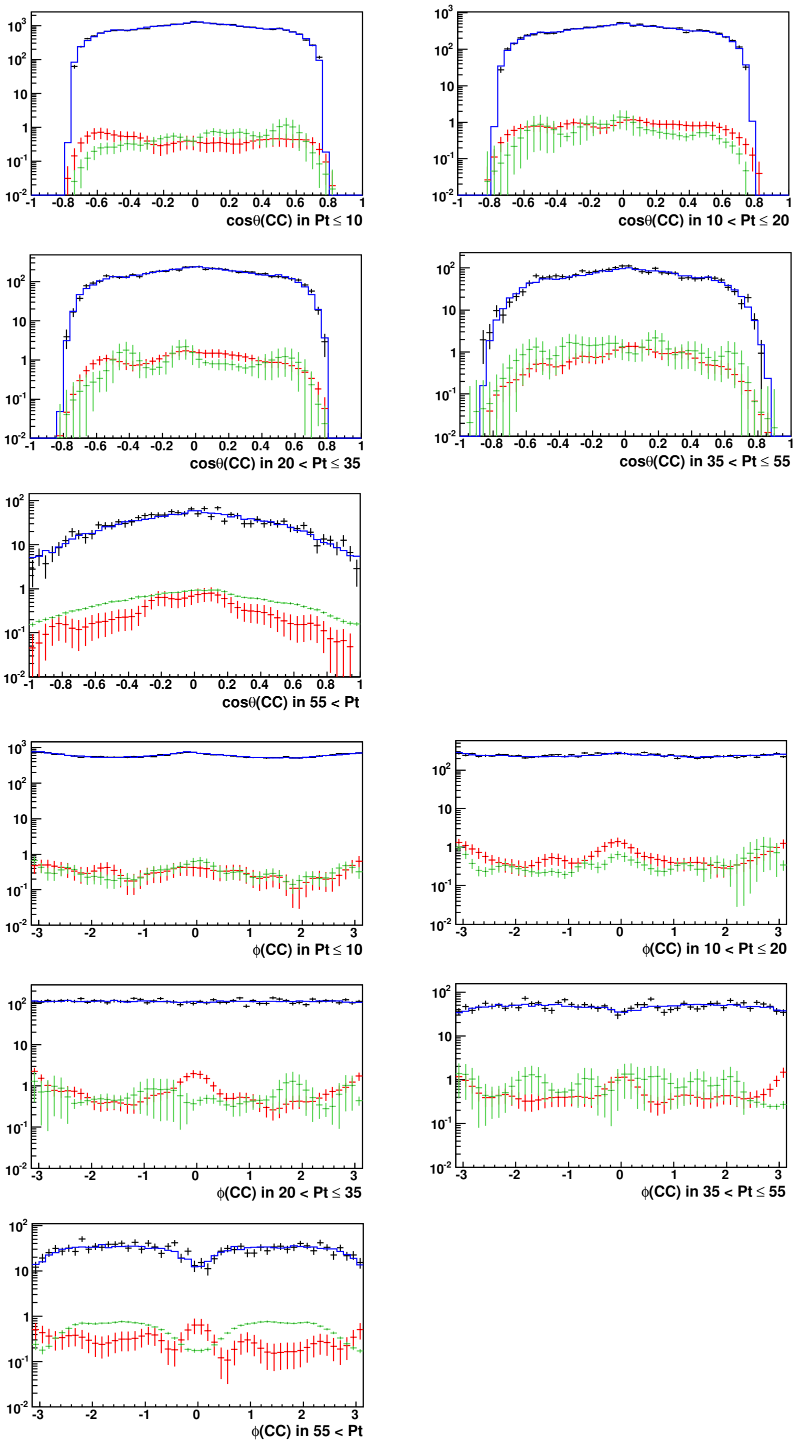

Figure 17: $\cos\theta$ and ϕ distribution of data, CDF PYTHIA MC, and background contributions in each P_T bin for CC topology. The black crosses are data, the blue histogram is CDF PYTHIA, the red crosses are QCD background, and the green crosses are Electroweak background.

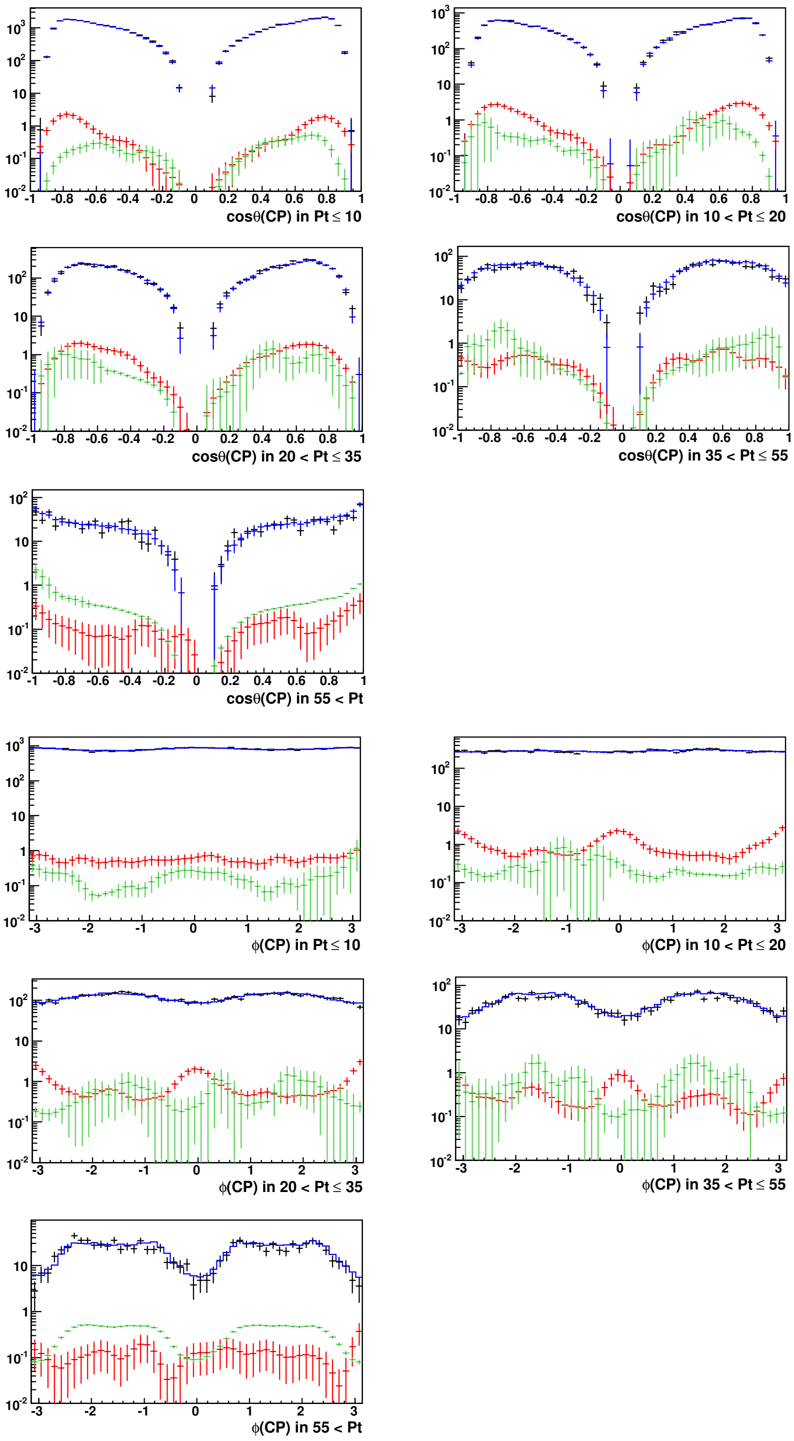

Figure 18: $\cos\theta$ and ϕ distribution of data, CDF PYTHIA MC, and background contributions in each P_T bin for CP topology. The black crosses are data, the blue histogram is CDF PYTHIA, the red crosses are QCD background, and the green crosses are Electroweak background.

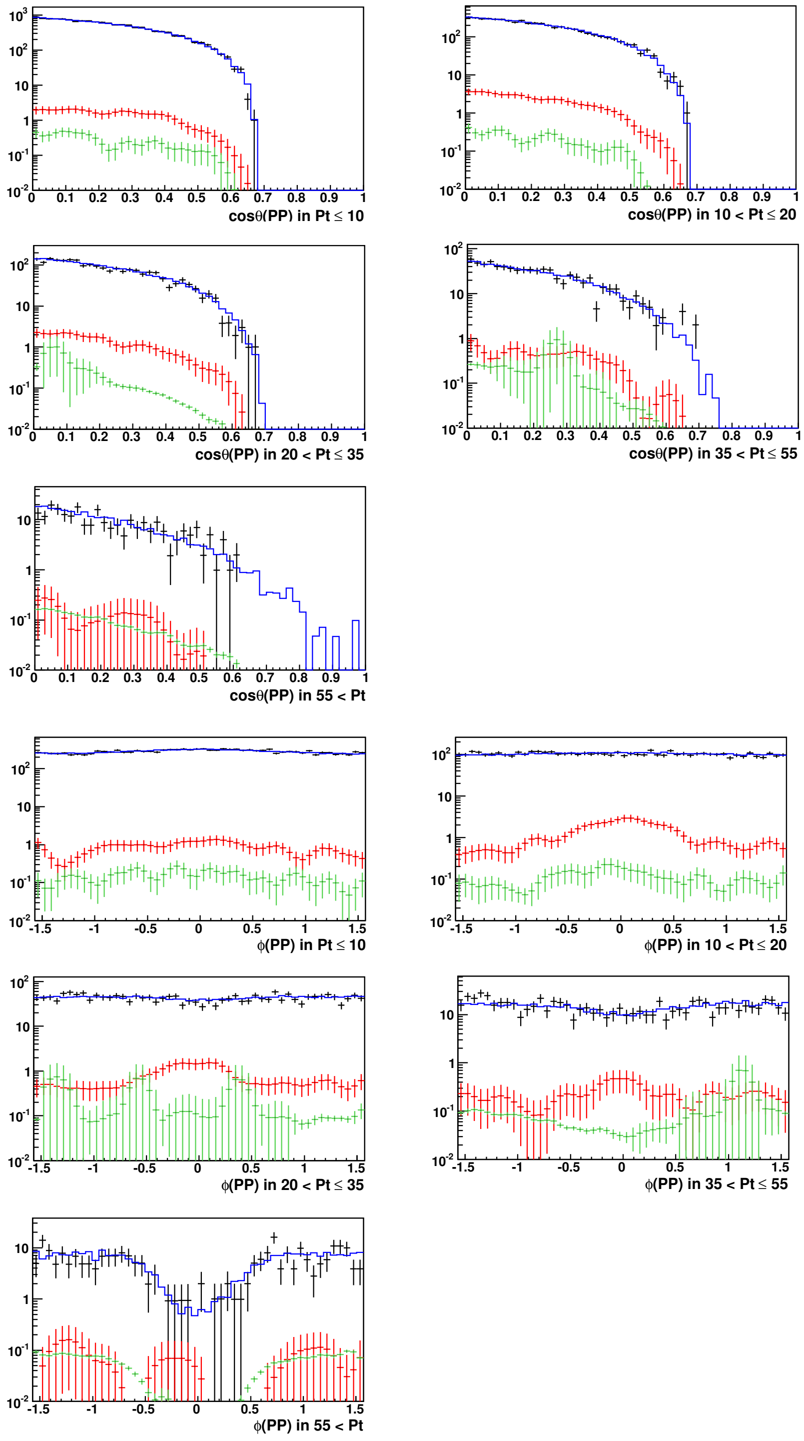

Figure 19: $\cos\theta$ and ϕ distribution of data, CDF PYTHIA MC, and background contributions in each P_T bin for PP topology. The black crosses are data, the blue histogram is CDF PYTHIA, the red crosses are QCD background, and the green crosses are Electroweak background.

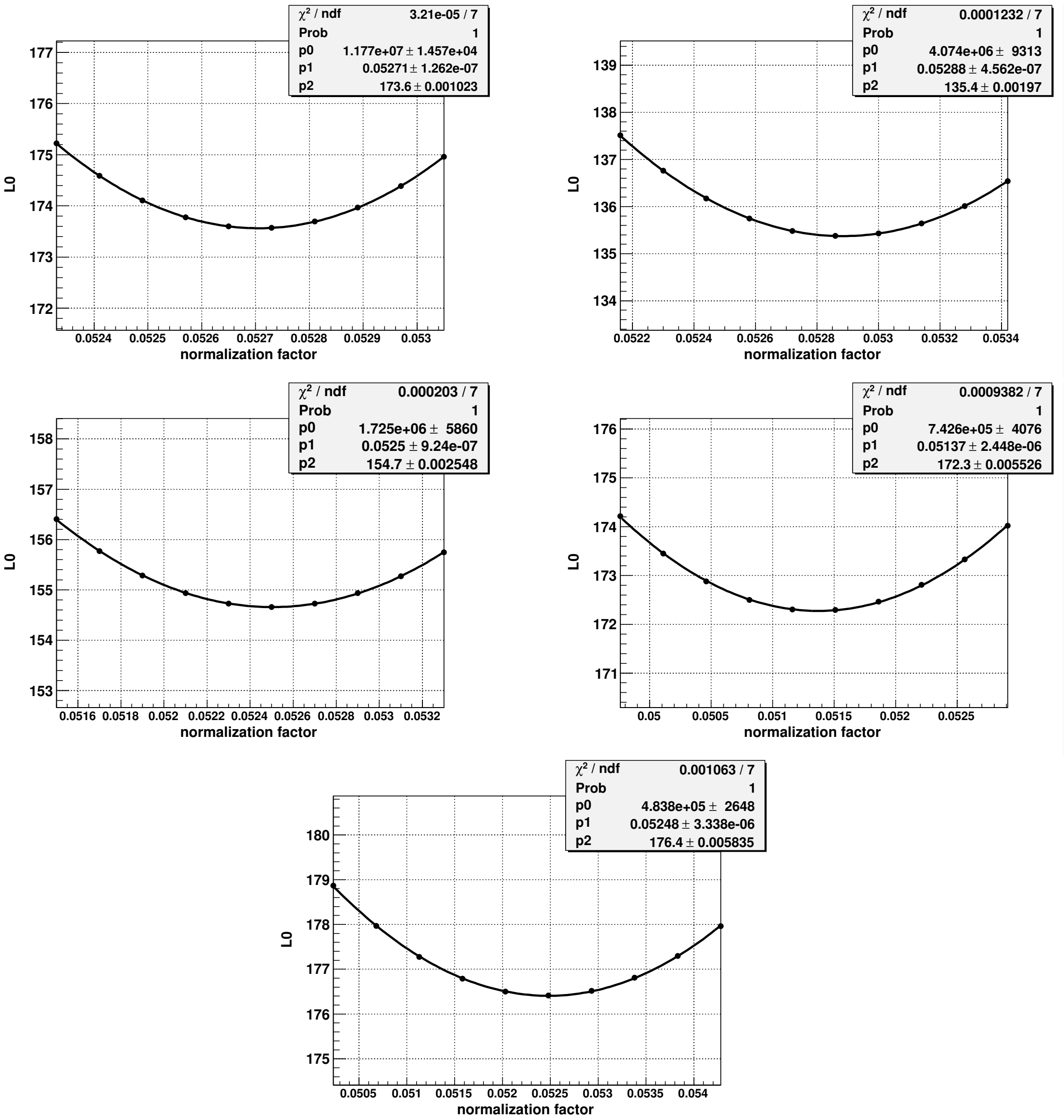

Figure 20: L_0 in the normalization factor, f, for Z P_{T} bin measured by $\cos\theta$ fitting. P_T bin, (0,10) corresponds to the top and left plot, (10,20) to top and right plot, (20,35) to the middle and left plot, (35,55) to the middle and right plot, (55 and above) to the bottom plot.

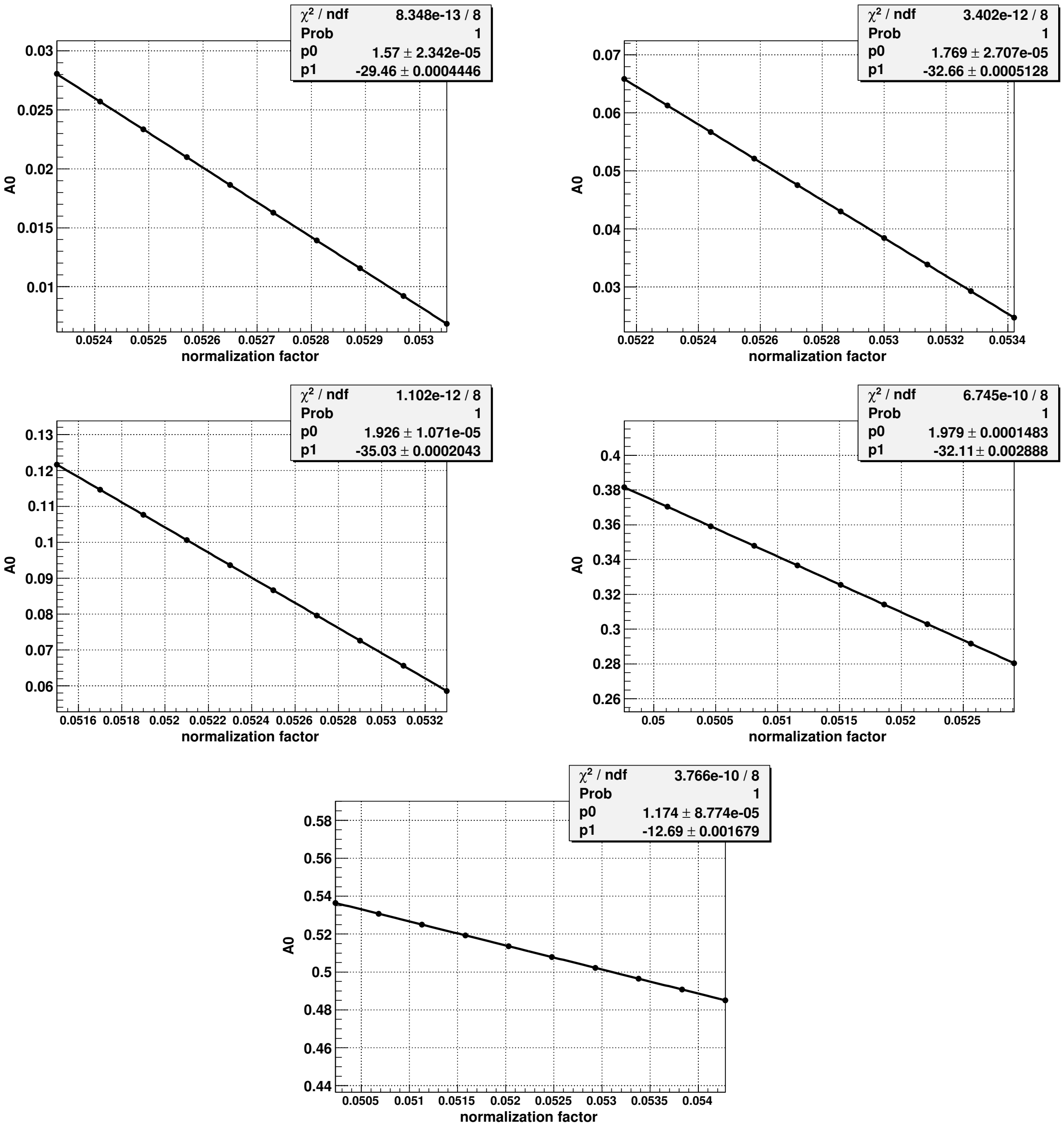

Figure 21: A_0 in the normalization factor, f, for Z P_{T} bin measured by $\cos\theta$ fitting. P_T bin, (0,10) corresponds to the top and left plot, (10,20) to top and right plot, (20,35) to the middle and left plot, (35,55) to the middle and right plot, (55 and above) to the bottom plot.

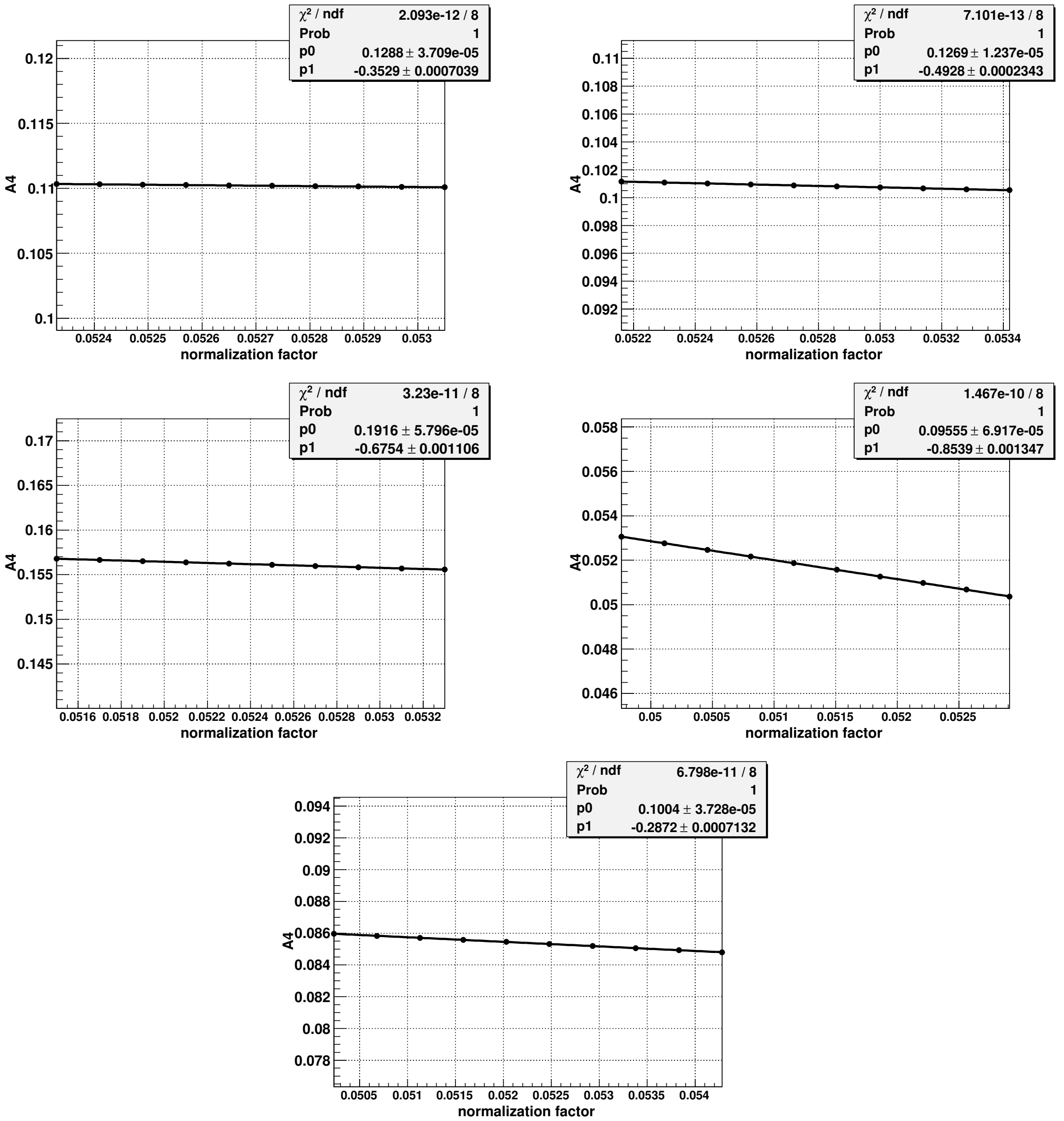

Figure 22: A_4 in the normalization factor, f, for Z P_{T} bin measured by $\cos\theta$ fitting. P_T bin, (0,10) corresponds to the top and left plot, (10,20) to top and right plot, (20,35) to the middle and left plot, (35,55) to the middle and right plot, (55 and above) to the bottom plot.

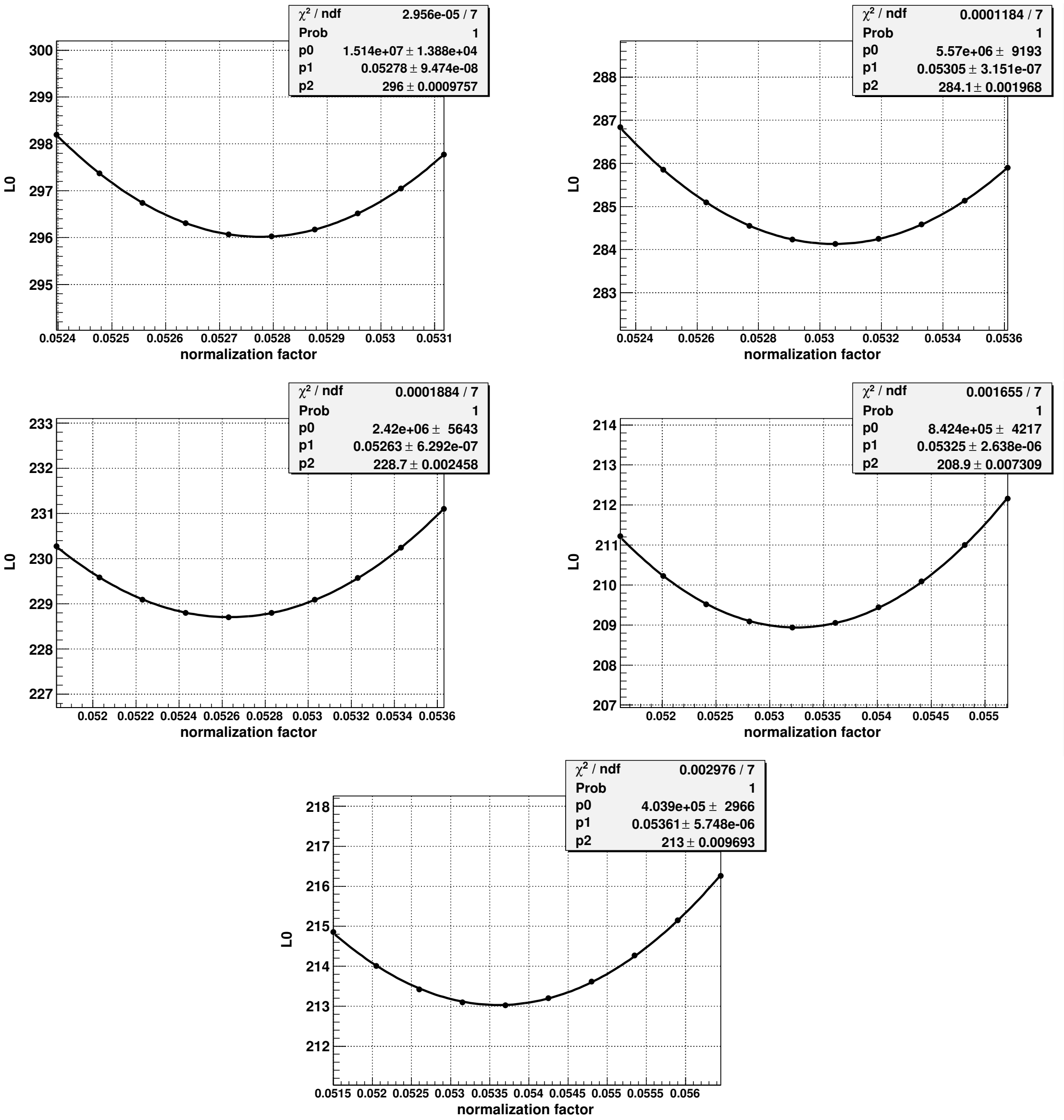

Figure 23: L_0 in the normalization factor, f, for Z P_{T} bin measured by ϕ fitting. P_T bin, (0,10) corresponds to the top and left plot, (10,20) to top and right plot, (20,35) to the middle and left plot, (35,55) to the middle and right plot, (55 and above) to the bottom plot.

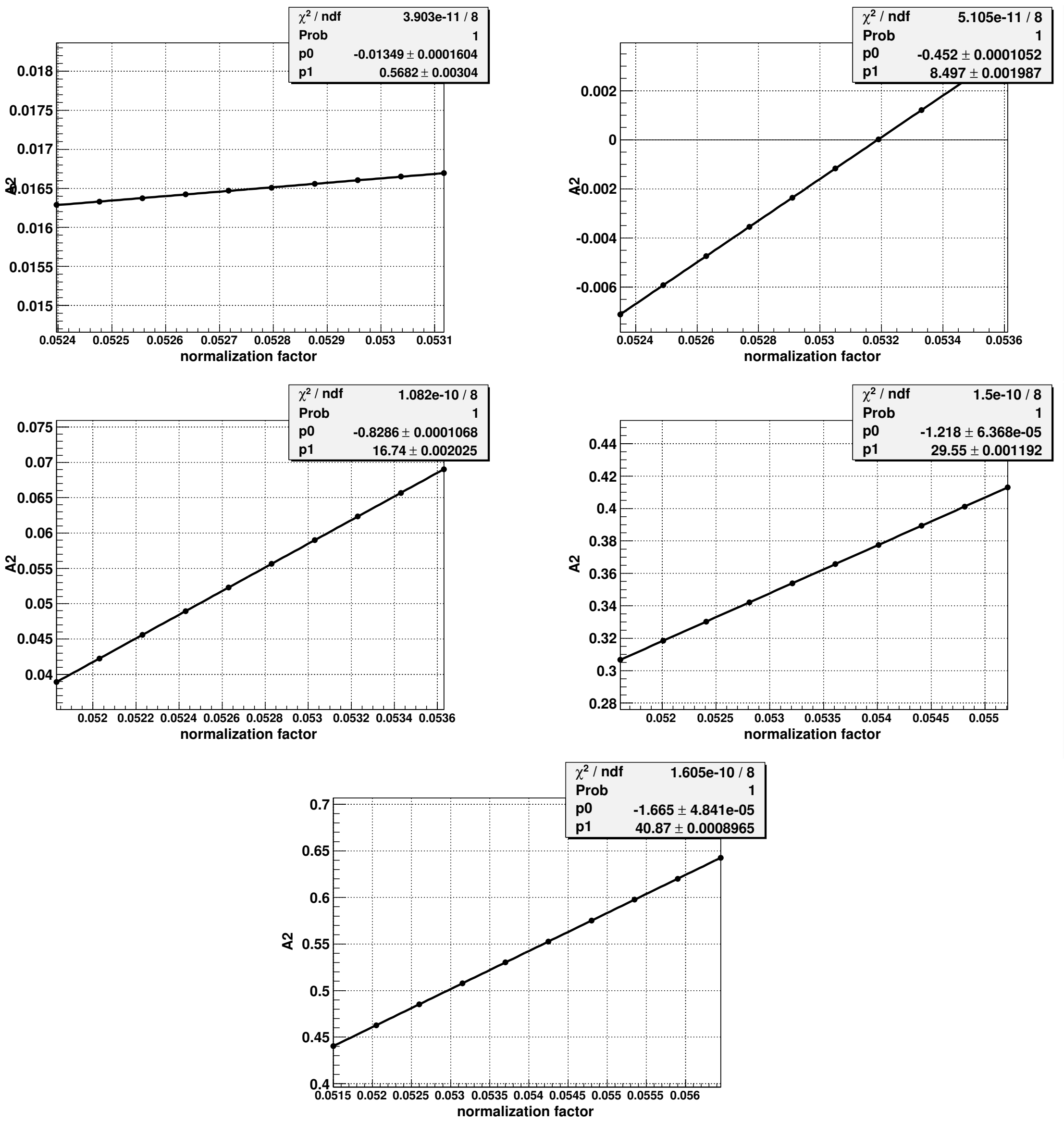

Figure 24: A_2 in the normalization factor, f, for Z P_{T} bin measured by ϕ fitting. P_T bin, (0,10) corresponds to the top and left plot, (10,20) to top and right plot, (20,35) to the middle and left plot, (35,55) to the middle and right plot, (55 and above) to the bottom plot.

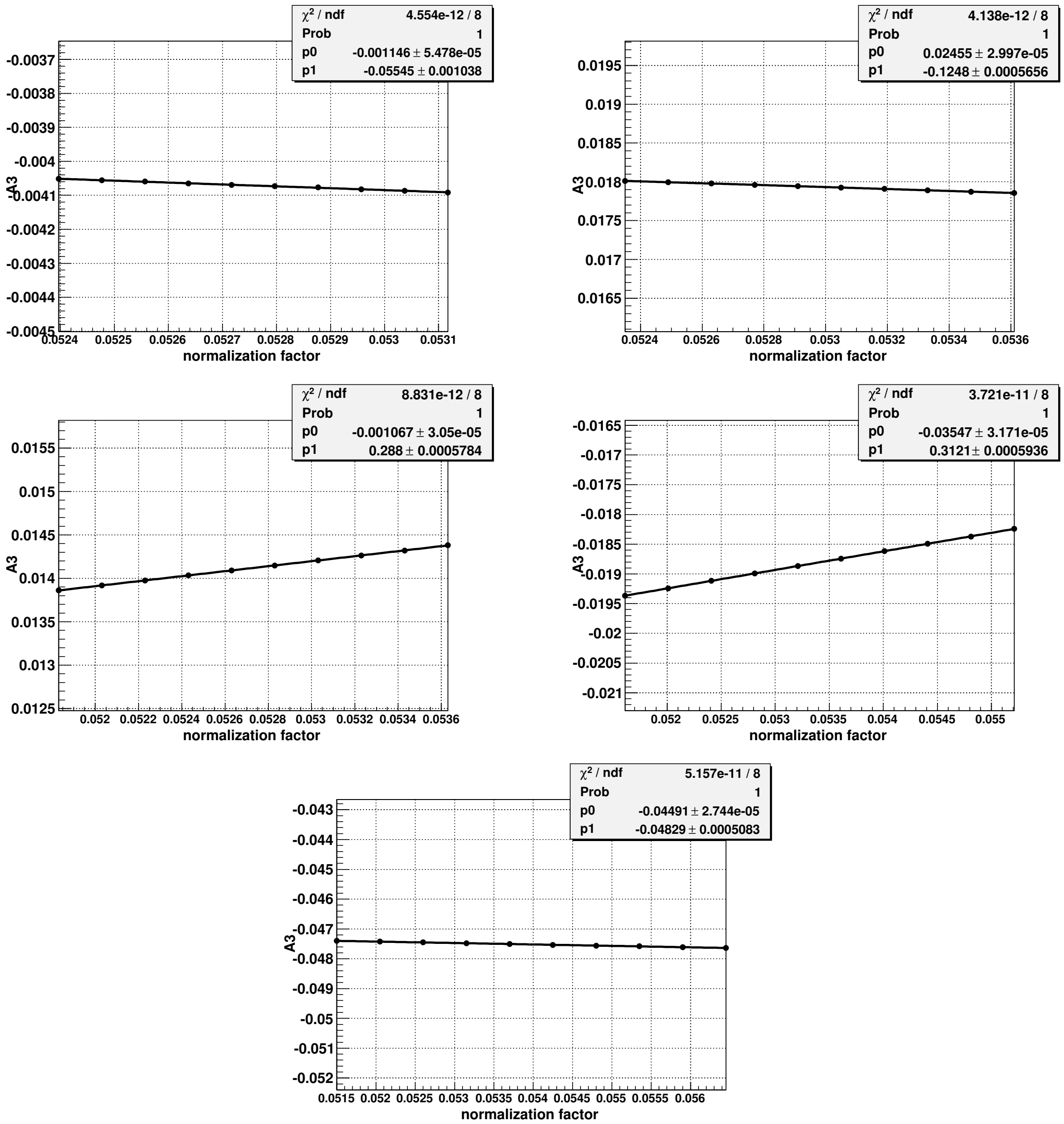

Figure 25: A_3 in the normalization factor, f, for Z P_{T} bin measured by ϕ fitting. P_T bin, (0,10) corresponds to the top and left plot, (10,20) to top and right plot, (20,35) to the middle and left plot, (35,55) to the middle and right plot, (55 and above) to the bottom plot.

	CDF PYTHIA Prediction	
P_{T} bin (GeV)	A_2	A_3
00–10 (4.8)	$(-.305 \pm .241)10^{-2}$	$(-.012 \pm .102)10^{-2}$
10–20 (14.1)	$(.179 \pm .041)10^{-1}$	$(.203 \pm .172)10^{-2}$
20–35 (26.0)	$(.691 \pm .059)10^{-1}$	$(.385 \pm .251)10^{-2}$
35–55 (42.9)	$.186 \pm .009$	$(.341 \pm .405)10^{-2}$
> 55 (73.7)	$.368 \pm .013$	$(-.169 \pm .577)10^{-2}$

	Data	
P_{T} bin (GeV)	A_2 CDF	A_3 CDF
00–10 (4.8)	$(.233 \pm .293(stat.))10^{-1}$	$(-.721 \pm .129)10^{-2}$
10–20 (14.1)	$(.172 \pm .384)10^{-1}$	$(.172 \pm .178)10^{-1}$
20–35 (26.0)	$(.984 \pm .572)10^{-1}$	$(.245 \pm .274)10^{-1}$
35–55 (42.9)	$.383 \pm .094$	$(.068 \pm .461)10^{-1}$
> 55 (73.7)	$.571 \pm .140$	$(-.479 \pm .627)10^{-1}$

Table 10: Fit parameters (A_2,A_3) to CDF PYTHIA prediction and data in boson P_{T} for the tight mass window, $85 < M_{ee} < 95 GeV/c^2$. The parameters, A_2 and A_3, are measured by fitting ϕ distribution. The CDF PYTHIA prediction before QED radiation (CDF MC). In the "P_{T} bin" column, the number in parenthesis is the mean P_{T} in the bin. The statistical uncertainty is only considered.

3.2.3 Goodness of the fit - data and MC comparison

To test the goodness of the fit, we compare the data with PYTHIA MC which is tweaked for the angular coefficients to have the best match with the data. For the comparison, we also compared the data with the default PYTHIA which has its own angular coefficients. This comparison is done for each P_{T} bin and the χ^2 test is described in section 2.5. The plots for the comparison are posted in this section. The CC topology is shown in Figure (26, 27, and 28), the CP topology in Figure (29, 30, and 31) , and the PP topology in Figure (32, 33, and 34).

(a) P_{T} bin : (0,10) in CC topology

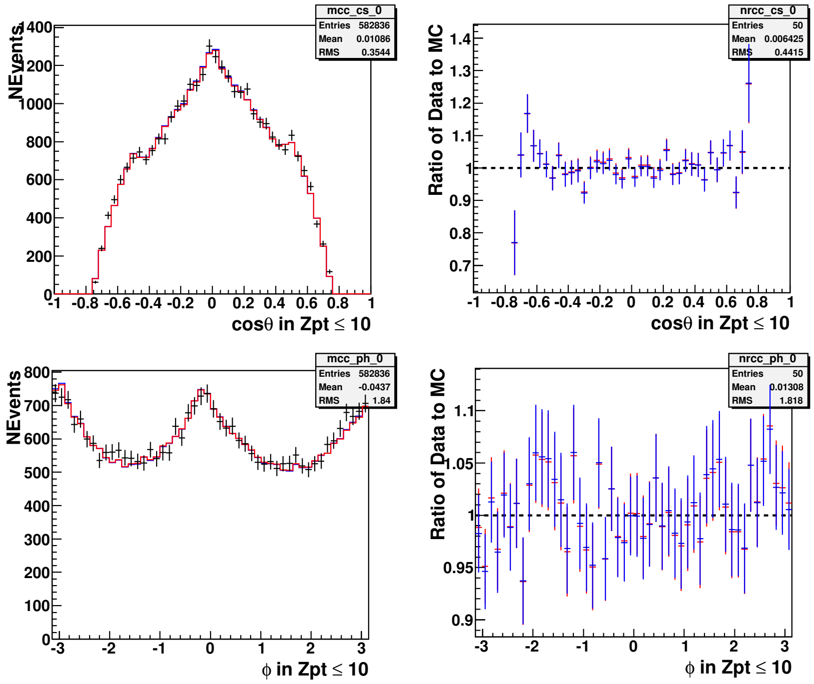

(b) P_{T} bin : (10,20) in CC topology

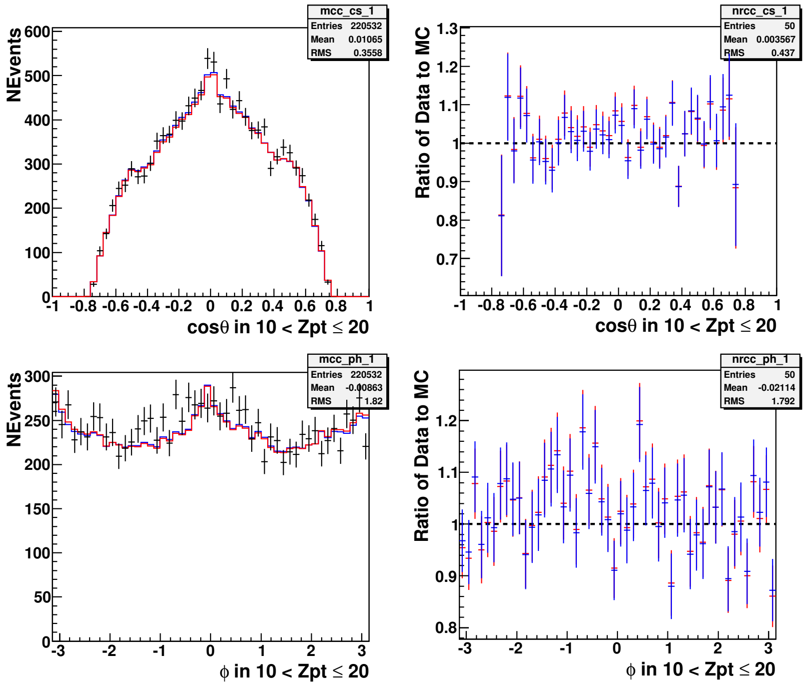

Figure 26: The $\cos\theta$ and ϕ distribution of CC topology in data and MC for P_{T} bin, (0,10) and (10,20). The plots in the left hand side show the angular distributions and the plots in the right hand side show the ratio of data to MC. The blue histograms and points correspond to the prediction which has a best match with the data and the red histograms and points correspond to PYTHIA default prediction.

(a) P_{T} bin : (20,35) in CC topology

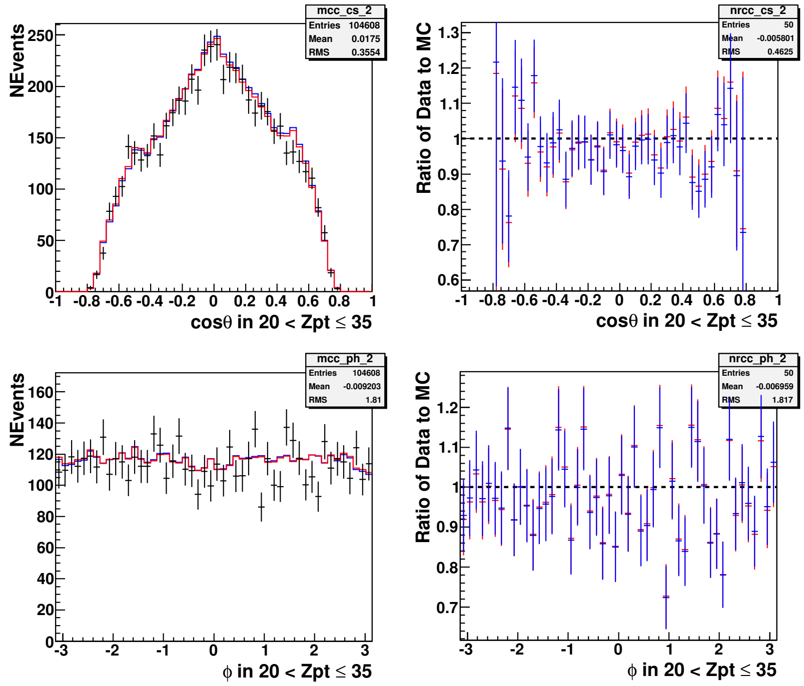

(b) P_{T} bin : (35,55) in CC topology

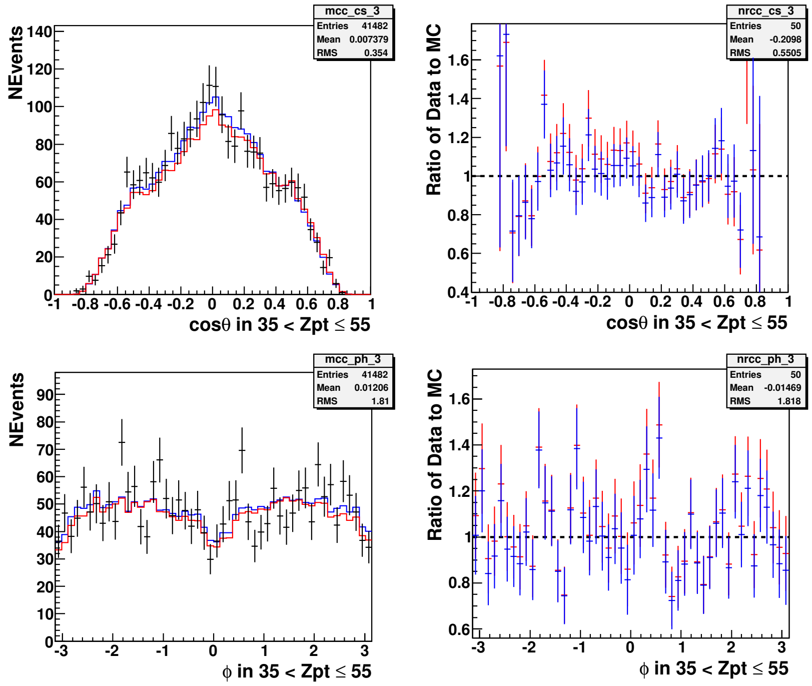

Figure 27: The $\cos\theta$ and ϕ distribution of CC topology in data and MC for P_{T} bin, (20,35) and (35,55). The plots in the left hand side show the angular distributions and the plots in the right hand side show the ratio of data to MC. The blue histograms and points correspond to the prediction which has a best match with the data and the red histograms and points correspond to PYTHIA default prediction.

(a) P_{T} bin : (55 and above) in CC topology

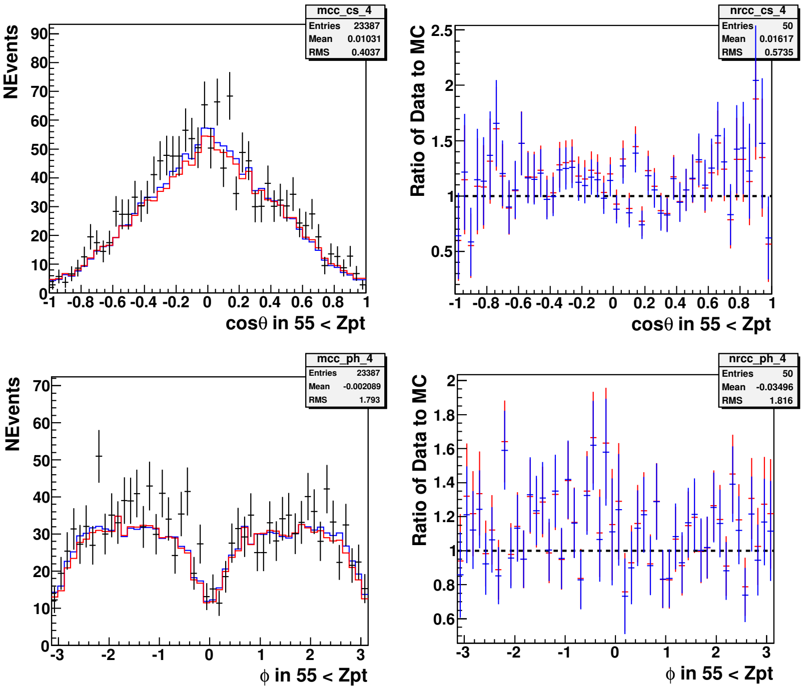

Figure 28: The $\cos\theta$ and ϕ distribution of CC topology in data and MC for P_{T} bin, (55 and above). The plots in the left hand side show the angular distributions and the plots in the right hand side show the ratio of data to MC. The blue histograms and points correspond to the prediction which has a best match with the data and the red histograms and points correspond to PYTHIA default prediction.

(a) P_{T} bin : (0,10) in CP topology

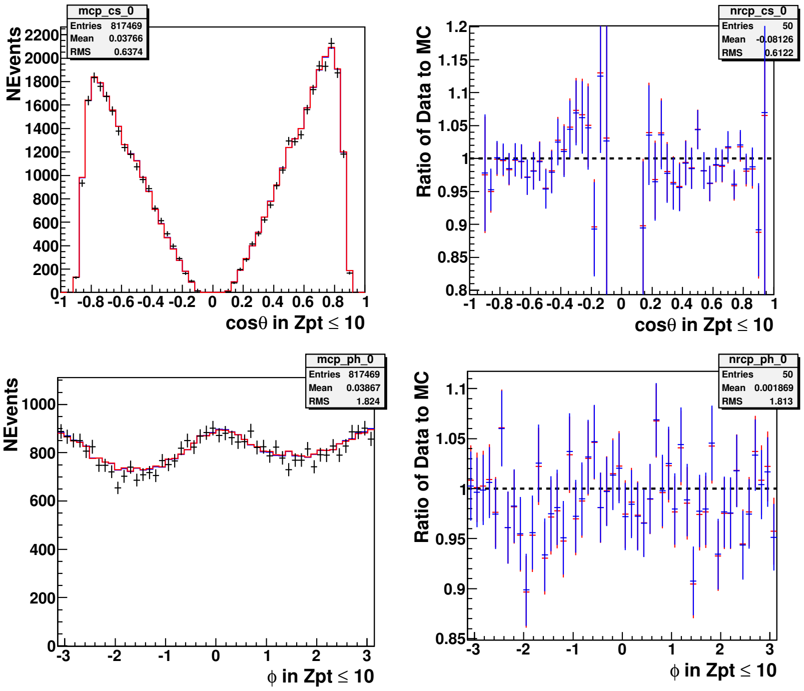

(b) P_{T} bin : (10,20) in CP topology

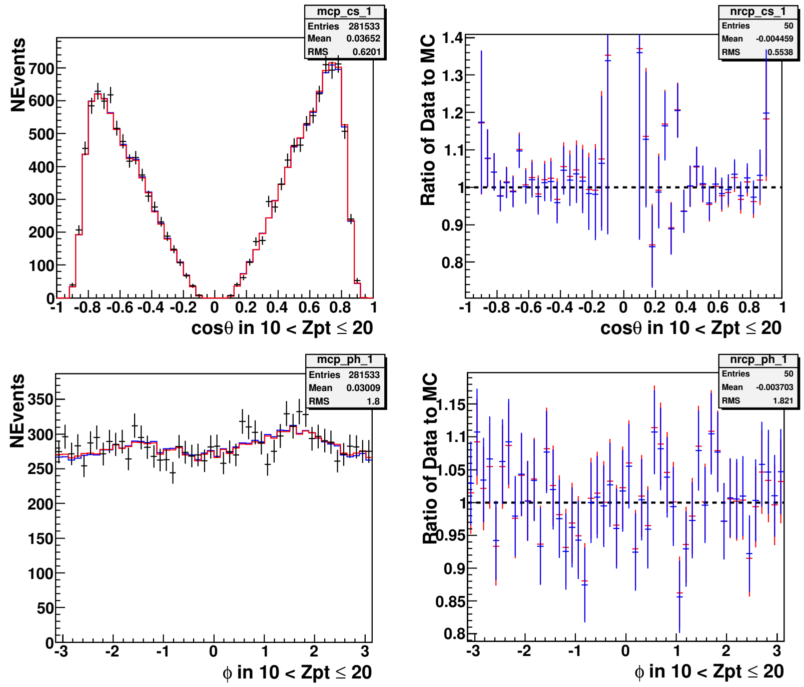

Figure 29: The $\cos\theta$ and ϕ distribution of CP topology in data and MC for P_{T} bin, (0,10) and (10,20). The plots in the left hand side show the angular distributions and the plots in the right hand side show the ratio of data to MC. The blue histograms and points correspond to the prediction which has a best match with the data and the red histograms and points correspond to PYTHIA default prediction.

(a) P_{T} bin : (20,35) in CP topology

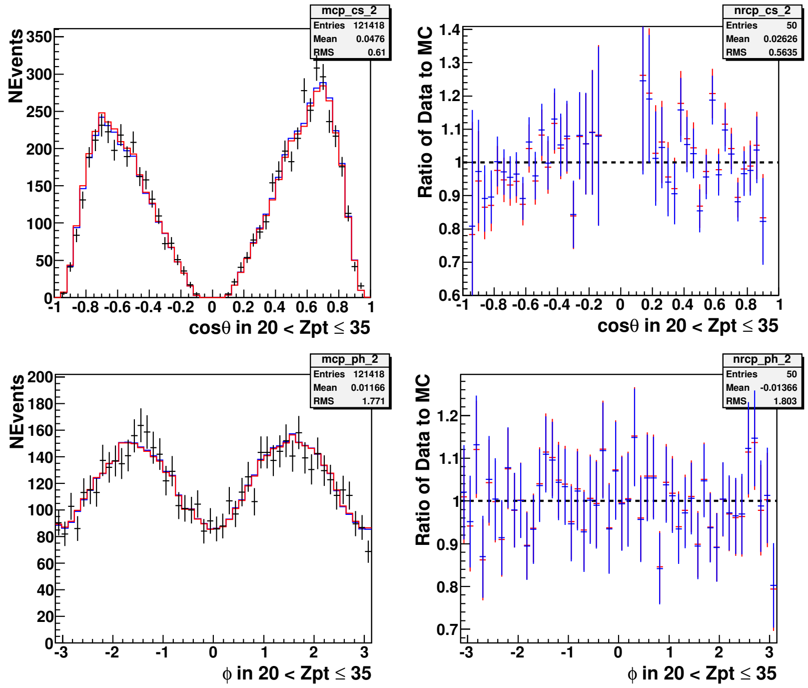

(b) P_{T} bin : (35,55) in CP topology

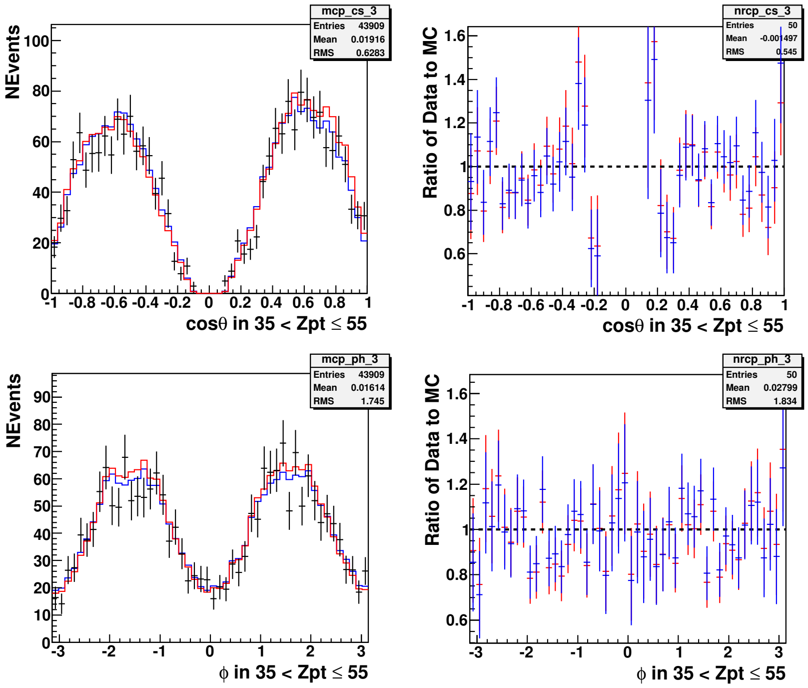

Figure 30: The $\cos\theta$ and ϕ distribution of CP topology in data and MC for P_{T} bin, (20,35) and (35,55). The plots in the left hand side show the angular distributions and the plots in the right hand side show the ratio of data to MC. The blue histograms and points correspond to the prediction which has a best match with the data and the red histograms and points correspond to PYTHIA default prediction.

(a) P_{T} bin : (55 and above) in CP topology

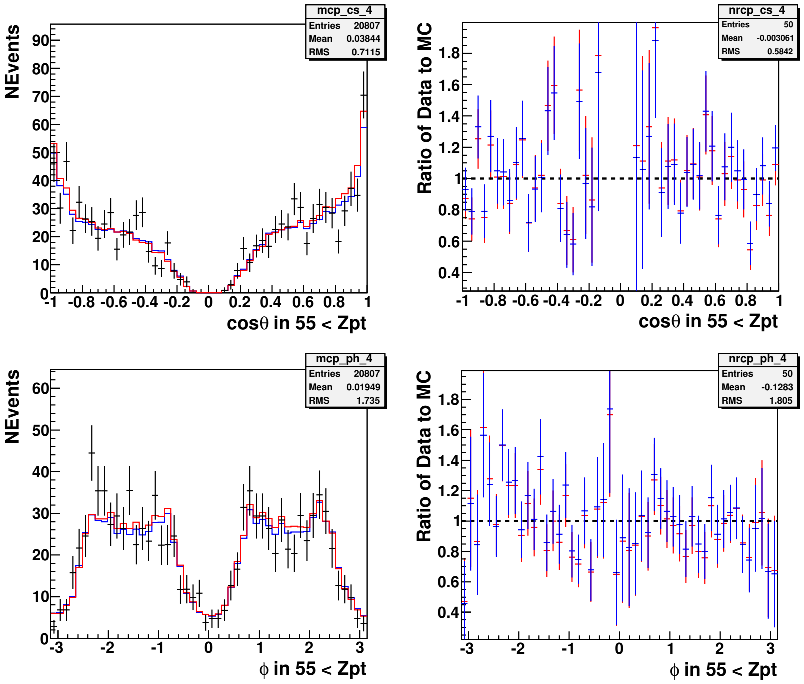

Figure 31: The $\cos\theta$ and ϕ distribution of CP topology in data and MC for P_{T} bin, (55 and above). The plots in the left hand side show the angular distributions and the plots in the right hand side show the ratio of data to MC. The blue histograms and points correspond to the prediction which has a best match with the data and the red histograms and points correspond to PYTHIA default prediction.

(a) P_{T} bin : (0,10) in PP topology

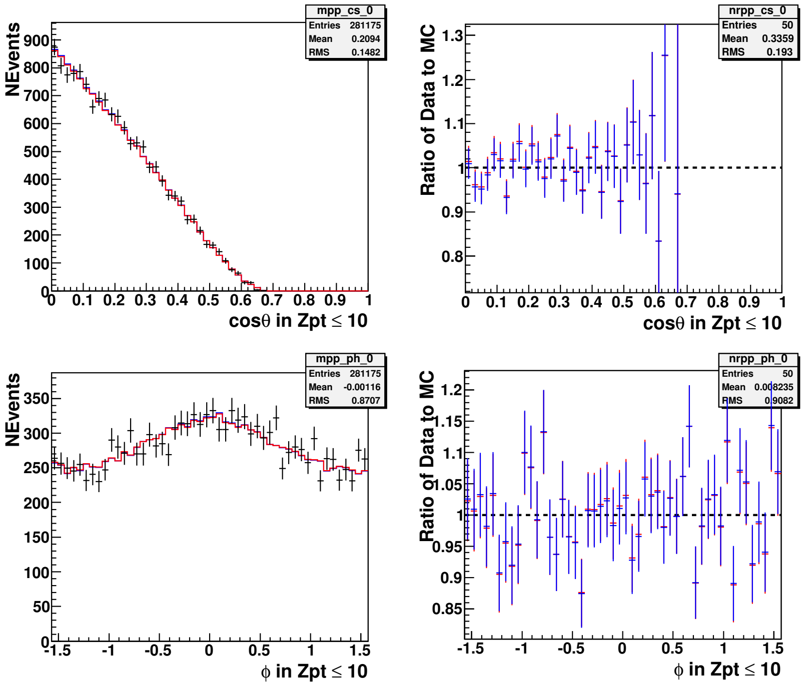

(b) P_{T} bin : (10,20) in PP topology

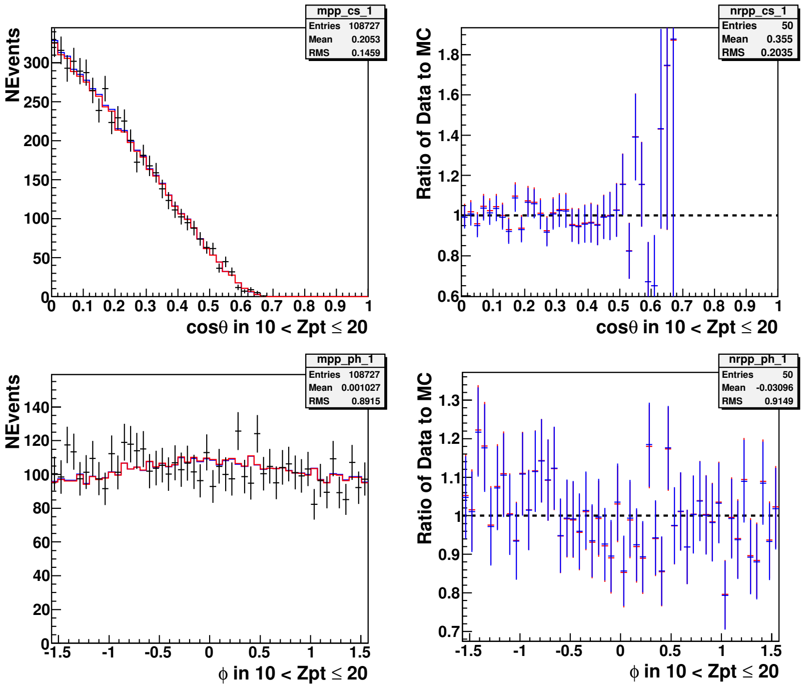

Figure 32: The $\cos\theta$ and ϕ distribution of PP topology in data and MC for P_{T} bin, (0,10) and (10,20). The plots in the left hand side show the angular distributions and the plots in the right hand side show the ratio of data to MC. The blue histograms and points correspond to the prediction which has a best match with the data and the red histograms and points correspond to PYTHIA default prediction.

(a) P_{T} bin : (20,35) in PP topology

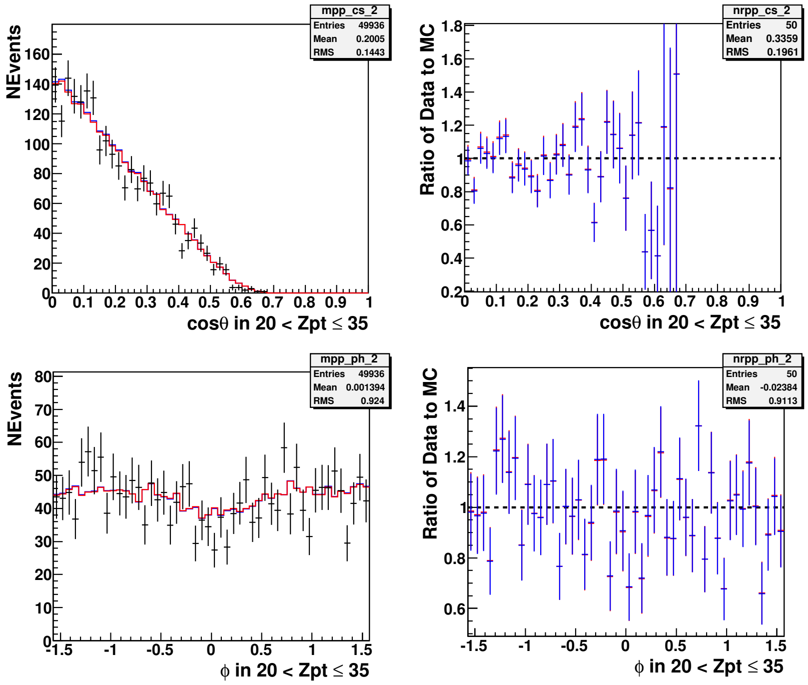

(b) P_{T} bin : (35,55) in PP topology

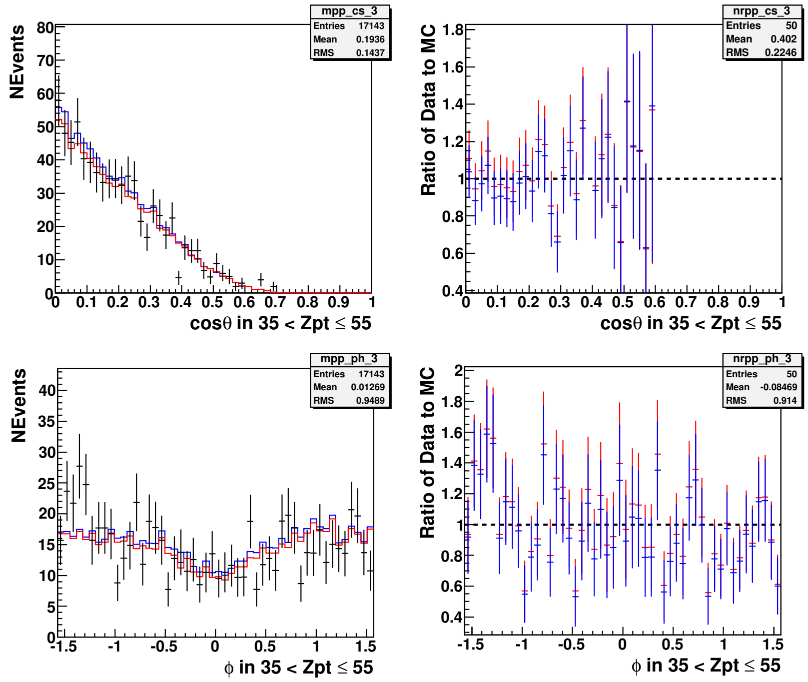

Figure 33: The $\cos\theta$ and ϕ distribution of PP topology in data and MC for P_{T} bin, (20,35) and (35,55). The plots in the left hand side show the angular distributions and the plots in the right hand side show the ratio of data to MC. The blue histograms and points correspond to the prediction which has a best match with the data and the red histograms and points correspond to PYTHIA default prediction.

(a) P_{T} bin : (55 and above) in PP topology

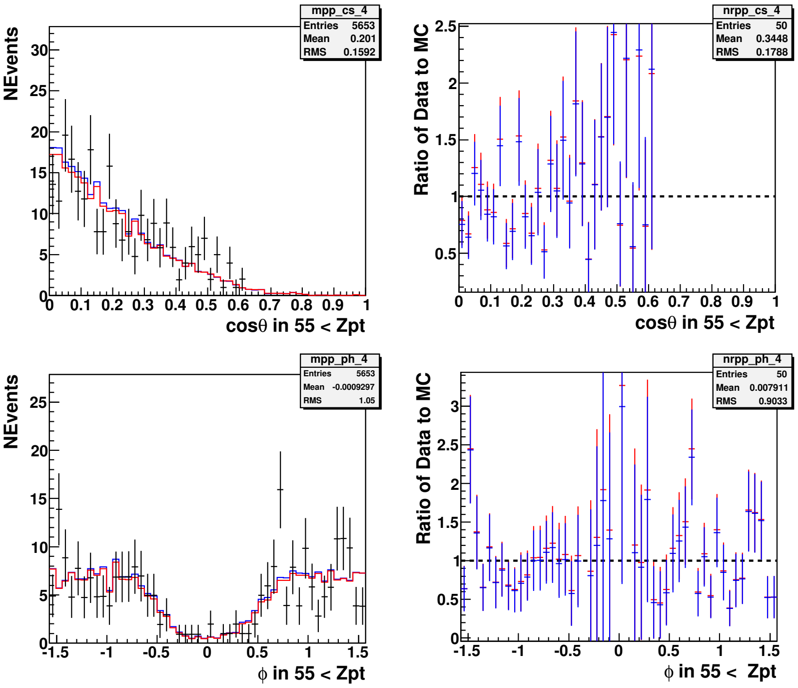

Figure 34: The $\cos\theta$ and ϕ distribution of PP topology in data and MC for P_{T} bin, (55 and above). The plots in the left hand side show the angular distributions and the plots in the right hand side show the ratio of data to MC. The blue histograms and points correspond to the prediction which has a best match with the data and the red histograms and points correspond to PYTHIA default prediction.

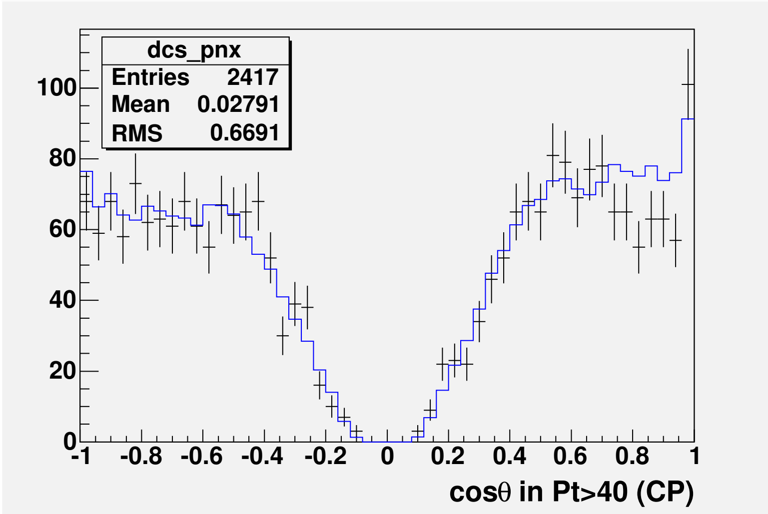

Figure 35: $\cos\theta$ distribution of CP topology in $P_{\mathrm{T}} > 40$ GeV. The black crosses are the data points and the blue histogram is PYTHIA MC in the reconstructed level. The data shows a systematic drop compared to MC in $\cos\theta > 0.7$.

3.3 $\cos\theta$ in high P_{T} for CP topology

The CP topology has more acceptance in large $|\cos\theta|$ region compared to other topologies. Especially, the acceptance of $P_T > 40$ region is 25% and flat in $0.50 < |\cos\theta| < 0.95$. During the study, we found that data has a systematic drop compared to MC in $\cos\theta > 0.7$ shown in Figure 35. This region has 4.0σ deviation between data and MC for the total number of events, which is not small difference and need to be investigated. First indication to debug this difference is to check the tracking efficiency based on the silicon detector geometry. We apply the tracking efficiency of the data into MC as a function of the number of the expected silicon layers which the electron passes through (nsil). Therefore, if MC doesn't describe the silicon detector geometry (for example, dead channels or fiduciality) well, it results in the shape difference of $\cos\theta$ or ϕ. First, we compare nsil distribution of data to MC in each P_T bin. Figure 36 shows the nsil distribution of 2 track events in $\cos\theta > 0$ and $\cos\theta < 0$. The negative $\cos\theta$ region shows a good agreement between data and MC, but the positive region shows that the data has less events in nsil=4,5, and 6 region. We also compare the nsil distribution in high $\cos\theta$ region and find the same level of difference shown in Figure 36.

To check if there is any silicon detector region which produces the sharp efficiency drop, we checked the event distribution separating the events based on the silicon detector geometry like the silicon detector barrel and wedge. Figure 37 shows the wedge distribution of the events of CP topology in $P_{\mathrm{T}} > 40$ GeV and $\cos\theta > 0.7$ where shows the deviation between the data and MC. In the plot, there is no specific region which describes the big deviation between the data and MC. Figure 38 also shows the barrel distribution which the track passes through. The selected events are same with the events shown in Figure 37. The top plot in Figure 38 corresponds

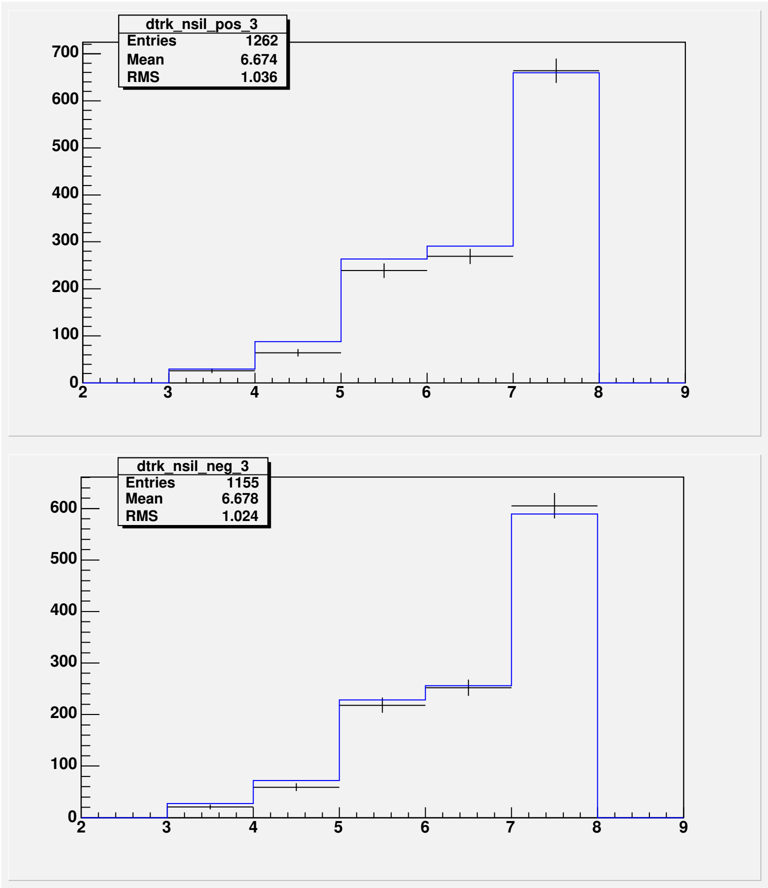

Figure 36: The nsil distribution in $P_{\mathrm{T}} > 40$ GeV. The top plot corresponds to the positive $\cos\theta$ region and the bottom plot corresponds to the negative $\cos\theta$ region. The black crosses are the data and the blue histograms are MC prediction.

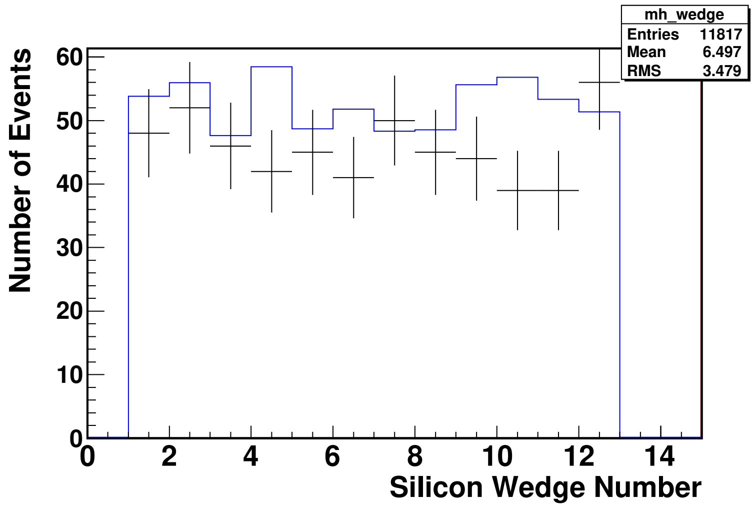

Figure 37: The wedge distribution which the track passes through. The selected events are in $P_{\rm T} > 40$ GeV and $\cos\theta > 0.7$. The black crosses are the data and the blue histograms are MC prediction.

to the barrel position which the track passes in the first silicon layer (layer 1) and the bottom plot corresponds to the barrel position which the track passes in the last silicon layer (layer 7). Like the wedge distribution, the barrel distributions also show that the overall tracking efficiency in data is a little bit lower than MC and any specific barrel region doesn't have the efficiency drop. Therefore, we conclude that the deviation shown in high $\cos\theta$ region doesn't come from the tracking efficiency.

The other possibility to explain the deviation is the acceptance. If MC doesn't describe the data for the kinematic distribution like η or E_T distribution in high $\cos\theta$, the difference is also shown in the final selected events. So, we compare the data and MC for the kinematic distributions, η, E_T, ZVertex, and dielectron mass. The kinematic distributions also show the reasonable agreement between the data and MC.

We also separate the data events into the run period and compare the shapes using KS-test to check if any special run period has the different $\cos\theta$ distribution, so it makes the event drop in high $\cos\theta$. However, KS-test gives the reasonable agreement among the run periods, so the event drop in data doesn't come from the run dependence.

For the last check, we make the fine bins in high $P_{\rm T}$ region and compare the number of events in each $P_{\rm T}$ bin between the data and MC to check if any specific $P_{\rm T}$ region makes the deviation. Table 11 summarizes the deviation in each $P_{\rm T}$ bin for the positive $\cos\theta$ ($\cos\theta > 0.7$) and the negative $\cos\theta$ ($\cos\theta < -0.7$) as a reference to compare. (The negative $\cos\theta$ region shows the good agreement between the data and MC.)
However, we find that the deviation in $\cos\theta > 0.7$ is shown in all high $P_{\rm T}$ region.

From all studies which was done to investigate the difference between the data

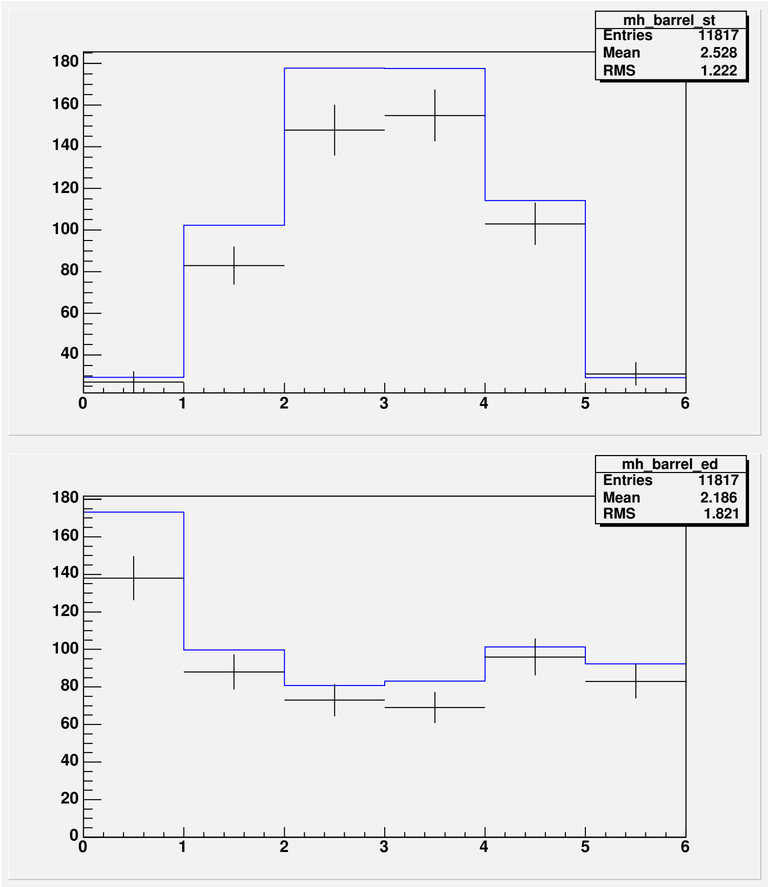

Figure 38: The barrel distribution which the track passes through. The selected events are in $P_{\mathrm{T}} > 40$ GeV and $\cos\theta > 0.7$. The top plot corresponds to the barrel position which the track passes in the first silicon layer (layer $= 0$) and the bottom plot corresponds to the barrel position which the track passes in the last silicon layer (layer $= 7$). The black crosses are the data and the blue histograms are MC prediction.

P_{T} bin (GeV)	$\cos\theta > 0.7$	$\cos\theta < -0.7$
> 40	-4.0σ	-0.7σ
35–40	-0.7σ	-1.5σ
40–55	-3.2σ	-0.4σ
> 55	-2.5σ	-0.6σ

Table 11: The deviation between the data and MC in P_{T} region.

and MC in $\cos\theta > 0.7$ for $P_{\mathrm{T}} > 40$ GeV, we conclude that the source of the deviation is likely the event fluctuation.

4 Appendix B - Derivation of LO formula for the angular coefficients.

We now show (following the derivation given in reference [9] that for the $q\bar{q} \to \gamma^*/Z \to \ell^+\ell^-$ annihilation diagram the perturbative calculation indicates that the angular coefficients originates from a kinematic effect which is a simple function of the angle of the proton and antiproton beams in the Collins-Soper frame. That angle is also a simple function of the transverse momentum P_T and mass $M_{\ell\ell}$ of the dilepton pair.

We start with the case of the emission of a single hard gluon by one of the partons. In this case, the dilepton has a finite value of P_T but we cannot determine if the gluon was emitted by the parton in the proton, or by the parton in the antiproton. All we know is that the dilepton pair has a finite transverse momentum in the laboratory system which is equal to the transverse momentum of the gluon.

If the gluon is emitted by the parton in the antiproton, than the parton level angular distribution (given below in $cos\theta'$) is with respect to the direction of the proton (which defines the quark-antiquark axis. If the gluon is emitted by the parton in the proton, then the parton level angular distribution (given below in $cos\theta'$) is with respect to the direction of the antiproton (which defines the quark-antiquark axis). The Collins-Soper frame splits this difference and takes the average direction (which happens to be the same as the laboratory z axis for colliding beam experiments).

In the derivation below, all vectors are defined in the Collins-Soper frame. We define unit vector $\mathbf{k}$ along the z axis, unit vector $\mathbf{i}$ along the x axis of the Collins-Soper frame (which is defined to be along the initial direction of the transverse momentum of the dilepton pair in the laboratory system). We also define a perpendicular unit vector $\mathbf{j}$ along the y axis. Here θ is the angle with respect to the z axis, and ϕ is defined in the $x - y$ plane.

In the Collins-Soper frame, the Drell-Yan pair is stationary and proton and antiproton move towards the dilepton pair with an angle ξ with respect to the z axis. In the Collins-Soper, we see an antiproton moving from the left at an angle ξ with respect to the z axis (in the $x - z$ plane), and a proton moving from the right with an angle$-\xi$ with respect to the z axis. The proton and antiproton form an isosceles triangle with the two beam particles (which have equal momentum p) intersecting at an angle $2\alpha = \pi - 2\xi$. Here $cos\ \alpha = sin\ \xi$. It can be easily shown that

$$\begin{aligned} sin^2\ \xi &= \frac{P_T^2}{P_T^2 + M_{\ell\ell}^2} \\ cos\ \xi &= \frac{M_{\ell\ell}}{(P_T^2 + M_{\ell\ell}^2)^{1/2}} \end{aligned} \tag{21}$$

In the Collins-Soper frame, we define a unit vector $\mathbf{Z'}$ along the direction of one of the beam particles (e.g. the proton). We define a unit vector $\mathbf{r}$ along the direction of Drell-Yan pair decay positron. We then obtain the following relations.

$$\begin{aligned} \mathbf{Z'} &= cos\xi\ \mathbf{k} + sin\xi\ \mathbf{i} \\ \mathbf{r} &= sin\theta\ cos\phi\ \mathbf{i} + sin\theta\ sin\phi\ \mathbf{j} + cos\theta\ \mathbf{k} \end{aligned} \tag{22}$$

$$
\begin{aligned}
cos\theta' &= \mathbf{r}\cdot\mathbf{Z'} \\
&= cos\xi\ cos\theta + sin\xi\ sin\theta\ cos\phi
\end{aligned}
$$

For the case for which the gluon was emitted by the parton in the antiproton, the angular distribution of the decay positron with respect to the Z' proton axis (which defines the quark-antiquark axis) is given by the simple expression.

$$
\frac{d\sigma}{dcos(\theta)} = A\left[(1+cos^2\theta') + \frac{B'}{A}cos\theta'\right] \tag{23}
$$

(if the gluon was emitted by the proton, then the above distribution is with respect to the direction of the antiproton which defines the quark-antiquark axis). Therefore, the distributions for the proton direction and for the antiproton direction should be added. Each should be weighted by the probability that the quark emitted the gluon $P_q(x_1)$, or the probability that the antiquark emitted a gluon, $P_{\bar{q}}(x_2)$. Here $P_q(x_1)$+$P_{\bar{q}}(x_2)$=1. For proton-antiproton collisions, the two probabilities should be equal. For proton-proton collisions, they could be different.

The proton direction is at an angle ξ. The antiproton direction angle is $-\xi$. If we plug in the expression for $cos\theta'$ from equation 23 into equation 23, we get

$$
\begin{aligned}
\frac{d\sigma}{dcos(\theta')} &= term_q + term_{\bar{q}} \qquad (24) \\
term_q &= A\ P_q(x_1)[1 + cos^2\theta\ cos^2\xi \\
&+\ sin^2\theta\ sin^2\xi\ cos^2\phi + \\
&+\ 2cos\xi\ cos\theta sin\xi\ sin\theta\ cos\phi \\
&+\ \frac{B'}{A}\ cos\xi\ cos\theta \\
&+\ sin\xi\ sin\theta\ cos\phi] \\
term_{\bar{q}} &= CP_{\bar{q}}(x_2)[1 + cos^2\theta\ cos^2\xi \\
&+\ sin^2\theta\ sin^2\xi\ cos^2\phi + \\
&-\ 2cos\xi\ cos\theta sin\xi\ sin\theta\ cos\phi \\
&+\ \frac{B'}{A}\ cos\xi\ cos\theta \\
&-\ \frac{B'}{A}\ sin\xi\ sin\theta\ cos\phi]
\end{aligned}
$$

Adding $term_q$ and $term_{\bar{q}}$ and defining $\Delta P = (P_q(x_1) - P_{\bar{q}}(x_2)) \approx 0$ we get

$$
\begin{aligned}
\frac{d\sigma}{dcos(\theta)} &= A\ [1 + cos^2\theta\ cos^2\xi \qquad (25) \\
&+\ sin^2\theta\ sin^2\xi\ cos^2\phi + \\
&+\ \Delta P\ 2cos\xi\ cos\theta\ sin\xi\ sin\theta\ cos\phi \\
&+\ \frac{B'}{A}\ cos\xi\ cos\theta \\
&+\ \Delta P\frac{B'}{A}\ sin\xi\ sin\theta\ cos\phi]
\end{aligned}
$$

using trigonometric identities

$$\begin{aligned} sin2\theta &= 2\ sin\theta\ cos\theta \\ cos^2\phi &= \frac{1}{2}(1 + cos2\phi) \end{aligned} \tag{26}$$

we rewrite equation 25 as:

$$\begin{aligned} \frac{d\sigma}{dcos(\theta)} &= A[1 + cos^2\theta) \\ &+ \frac{sin^2\xi}{2}(1 - 3cos^2\theta) \\ &+ \Delta P\ 2cos\xi sin\xi\ sin2\theta\ cos\phi \\ &+ \frac{sin^2\xi}{2}\ sin^2\theta\ cos2\phi \\ &+ \Delta P\frac{B'}{A}\ sin\xi\ sin\theta\ cos\phi \\ &+ \frac{B'}{A}\ cos\xi\ cos\theta] \end{aligned} \tag{27}$$

The general expression for the total differential cross section for dilepton pair production (e.g. Drell-Yan, $Z's$ or $W's$) in proton-antiproton (or proton-proton) collisions is given by:

$$\begin{aligned} \sigma &= A\ [(1 + \cos^2\theta) \\ &+ \frac{1}{2}A_0(1 - 3\cos^2\theta) + A_1 \sin 2\theta \cos\phi \\ &+ \frac{1}{2}A_2 \sin^2\theta \cos 2\phi + A_3 \sin\theta \cos\phi \\ &+ A_4 \cos\theta + A_5 \sin^2\theta \sin 2\phi \\ &+ A_6 \sin 2\theta \sin\phi + A_7 \sin\theta \sin\phi] \end{aligned} \tag{28}$$

where $A_4 = \frac{B}{A}$. Comparing equation 27 to equation 28 we get:

$$\begin{aligned} A_0 &= sin^2\xi = \frac{P_T^2}{P_T^2 + M_{\ell\ell}^2} \\ A_1 &= \Delta P\ cos\xi\ sin\xi = \Delta P\ \frac{P_T M_{\ell\ell}}{P_T^2 + M_{\ell\ell}^2} \approx 0 \\ A_2 &= \sin^2\xi = \frac{P_T^2}{P_T^2 + M_{\ell\ell}^2} \\ A_3 &= \Delta P\frac{B'}{A}\ sin\xi = \Delta P\frac{B'}{A}\frac{P_T}{(P_T^2 + M_{\ell\ell}^2)^{1/2}} \approx 0 \\ A_4 &= \frac{B}{A} = \frac{B'}{A}\ cos\xi = \frac{B'}{A}\frac{M_{\ell\ell}}{(P_T^2 + M_{\ell\ell}^2)^{1/2}} \\ \frac{B}{B'} &= \frac{M_{\ell\ell}}{(P_T^2 + M_{\ell\ell}^2)^{1/2}} \\ A_5 &= A_6 = A_7 = 0 \end{aligned} \tag{29}$$

Where B is the $cos\theta$ angular coefficient for quarks bound in the proton, and B' is the $cos\theta$ angular coefficient for free quarks. As far as we know, this is the first closed form derivation of the QCD corrections to the forward backward asymmetry (i.e. the expression above for A_4 and $\frac{B}{B'}$). The above perturbative formulae for A_0 and A_2 for the annihilation diagram for Drell-Yan production was first derived by Collins in 1979[6]. The perturbative expressions for A_0, A_1 and A_2 and ΔP (but not for A_3 and A_4) were also derived in a paper by Daniel Boer and Werner Vogelsang in 2006)[6]. The above expressions for A_0 and A_2 were shown to hold for the quark-antiquark annhilation diagram for all orders (resummation) by Berger et. al. in 2007[7].

In conclusion, if the Z/DY cross section is dominated by quark-antiquark annihilation (as expected) the perturbative calculation gives predictions for A_0 $(= A_2)$ and A_4 as the only surviving non zero angular coefficients. The simple QCD predictions for the angular coefficients are:

$$\begin{aligned} h(\theta, M_{\ell\ell}, P_T) &= \frac{1}{2}A_0(1-3\cos^2\theta) \\ A_0 &= sin^2\xi \\ sin^2\xi &= \frac{P_T^2}{P_T^2+M_{\ell\ell}^2} \\ A_4 &= \frac{B}{A} = \frac{B'}{A}\ cos\xi \\ \frac{B}{B'} &= cos\xi \\ cos\ \xi &= \frac{M_{\ell\ell}}{(P_T^2+M_{\ell\ell}^2)^{1/2}} \end{aligned} \tag{30}$$

The angular distributions predicted by standard Monte Carlo generators such as PHYTIA[11], ResBos resummation[18] and Vector Boson Production and Decay in Hadron Collisions Resummation VBP[19] for Z boson production at the Tevatron are well described by the above formulae.

On average, both QCD correction terms are very small. For Drell-Yan events the average ratio $P_T/M_{\ell\ell}$ is about 0.13 (e.g. 12 GeV P_T at the Z mass of 90 GeV). This implies that on average $< A_0(P_T) >= 0.018$, and $< \frac{B}{B'}(P_T >= 0.991$.

4.0.1 Method of Moments: An alternative way of extracting angular coefficients

In our analysis the angular coefficients $C_1 = A_0$ and $C_2 = B\ A_4$ are extracted from fits to the angular distributions.

Others have extracted the angular coefficients from the angles of the charged lepton of MC events by using the method of moments.

In this method the *moment* of a function $m(\theta, \phi)$ is defined as

$$< m(\theta,\phi) >= \frac{\int\int d\sigma(q_T, y, \theta, \phi) m(\theta,\phi) d\cos\theta d\phi}{\int\int d\sigma(q_T, y, \theta, \phi) d\cos\theta d\phi} \tag{31}$$

P_{T} bin (GeV)	QED Unfolding Factor ("C_1(*no QED*)"/"C_1 CDFmc")	
	PHYTHIA	estimate from equations 26
00–05(2.9)	0.050 ± 0.091	0.013
05–10 (7.2)	0.322 ± 0.076	0.140
10–20 (14.1)	0.410 ± 0.064	0.389
20–40 (27.5)	0.715 ± 0.038	0.723
> 40(60.1)	0.936 ± 0.024	0.953
40–60(50)	0.927 ± 0.038	0.919
60–80	0.953 ± 0.040	0.975
> 80	0.950 ± 0.034	

Table 12: Mass region $66 < M_{ee} < 116$. The correction factor that corrects the raw values of C_1 for QED effects for each P_{T} bin. The correction factor is calculated using the C_1 parameters shown in Table 1. "C_1(*no QED*)" in Table 1 is PYTHIA with no QED radiation and "C_1 CDFmc" is CDF standard PYTHIA with the QED radiation. This correction is compared to estimate from equations 16 with $\delta = 0.1$.

$$
\begin{aligned}
< m_0 > &\equiv < \frac{1}{2}(1 - 3\cos^2\theta) >= \frac{3}{20}(A_0 - \frac{2}{3}) \\
< m_1 > &\equiv < \sin 2\theta \cos\phi >= \frac{1}{5}A_1 \\
< m_2 > &\equiv < \sin^2\theta \cos 2\phi >= \frac{1}{10}A_2 \\
< m_3 > &\equiv < \sin\theta \cos\phi >= \frac{1}{4}A_3 \\
< m_4 > &\equiv < \cos\theta >= \frac{1}{4}A_4 \\
< m_5 > &\equiv < \sin^2\theta \sin 2\phi >= \frac{1}{5}A_5 \\
< m_6 > &\equiv < \sin 2\theta \sin\phi >= \frac{1}{5}A_6 \\
< m_7 > &\equiv < \sin\theta \sin\phi >= \frac{1}{4}A_7
\end{aligned}
\tag{32}
$$

For a set of data or Monte Carlo events, the integrals of Equation (31) are substituted by sums and the cross section expression is replaced by the weights w_i of the Monte Carlo events.

$$
< m(\theta, \phi) >= \frac{\sum_{i=1}^{N} m(\theta_i, \phi_i) w_i}{\sum_{i=1}^{N} w_i} \tag{33}
$$

Equations (32) are then solved for the angular coefficients (substituting the moments with the discrete expressions (33).

4.0.2 Derivation of the Collins-Soper angle ξ

For completeness, We now derive an expression for ξ as follows. In the lab, the dilepton moves in the transverse direction to the beam with $P_T = \ \gamma_T\beta_T\ M_{\ell\ell}$. Therefore in the rest frame of the Drell-Yan pair, the proton-antiproton system moves in the transverse direction towards dilepton with the same transverse velocity, i.e. with $\gamma_T\beta_T \ = P_T/M_{\ell\ell}$. The transverse momentum of the beam proton in this frame is $P_T^p = \gamma_T\beta_T \ \cdot E_{p,lab}$. The transverse momentum of the beam antiproton in this frame is $P_T^{\bar{p}} = \gamma_T\beta_T \ \cdot E_{\bar{p},lab}$. For $y = 0$ we have.

$$
\begin{aligned}
\gamma_T\beta_T &= P_T/M_{\ell\ell} \qquad (34)\\
\beta_T^2 &= \frac{P_T^2/M_{\ell\ell}^2}{1+P_T^2/M_{\ell\ell}^2}\\
P_T' &= P^p_{T,csframe,y=0}\\
&= \gamma_T\beta_T \ \cdot E^p_{lab}\\
&= (P_T/M_{\ell\ell})\cdot E^p_{lab}\\
P_z' &= P^p_{z,csframe,y=0}\\
&= P^p_{lab}\\
sin^2\xi &= \frac{(P_T')^2}{(P_z')^2+(P_T')^2}\\
sin^2\xi &= \frac{P_T^2/M_{\ell\ell}^2}{1+P_T^2/M_{\ell\ell}^2}
\end{aligned}
$$

where for relativistic hadron-collider energies we have set $E_{p-lab} = P_{p-lab}$.

For finite values of y we boost to the Collins-Soper in two steps. First we boost along the z direction in the lab such that the dilepton pair has zero momentum along the z axis. We call that the moving lab frame. Then we boost along the y (P_T) direction. The second boost is the described by equation above, except that the that the energy and momenta are evaluated in the moving lab frame. As long as the proton and antiproton beams are relativistic in this moving lab frame (which is indeed the case at Tevatron energies) the same expression holds.

4.0.3 Transforming to the Collins-Soper

IN the lab, we define unit vector **k** along the positive z axis, unit vector **i** a along the x axis (which is the direction of the transverse momentum of the dilepton pair in the laboratory system (and is also the z direction in the Collins-Soper frame) and unit vector **j** along the y axis. The momentum of the dielpton in the laboratory is P_z and a tranverse momentum P_x.

We write the momentum components of the lepton in the laboratory system as ℓ^x, ℓ^y, ℓ^z, ℓ^0,

To go to the center of mass of the dilepton system we first do a Lorentz tansformation along the z direction with the following β_z and γ_z.

$$\gamma_z\beta_z = P_z/M_{\ell\ell} \qquad (35)$$

$$
\begin{aligned}
\beta_z^2 &= \frac{P_z^2/M_{\ell\ell}^2}{1+P_z^2/M_{\ell\ell}^2} \\
\ell_1^0 &= \gamma_z \ell^0 - \gamma_z \beta_z \ell^z \\
\ell_1^z &= \gamma_z \ell^z - \gamma_z \beta_z \ell^0 \\
\ell_1^x &= \ell^x, \qquad \ell_1^y = \ell^y
\end{aligned}
$$

Then we do Lorentz transformation along the x axis with with the following β_x and γ_x.

$$
\begin{aligned}
\gamma_x \beta_z &= P_x/M_{\ell\ell} \\
\beta_x^2 &= \frac{P_x^2/M_{\ell\ell}^2}{1+P_x^2/M_{\ell\ell}^2} \\
\ell_2^0 &= \gamma_x \ell_1^0 - \gamma_x \beta_x \ell_1^x \\
\ell_2^x &= \gamma_x \ell_1^x - \gamma_x \beta_x \ell_1^0 \\
\ell_2^z &= \ell_1^z, \quad \ell_2^y = \ell_1^y = \ell^y
\end{aligned}
\tag{36}
$$

Now r unit vector in the Collins-Soper frame polar coordinates:

$$
\begin{aligned}
\mathbf{r} &= sin\theta\ cos\phi\ \mathbf{i} + \ sin\theta\ sin\phi\ \mathbf{j} + \ cos\theta\ \mathbf{k} \\
\frac{\ell_2^x}{\ell_2^0} &= sin\theta\ cos\phi, \quad \frac{\ell_2^y}{\ell_2^0} = \ sin\theta\ sin\phi \\
\frac{\ell_2^z}{\ell_2^0} &= cos\theta, \qquad cos^2\phi = \frac{1}{2}(1+cos2\phi)
\end{aligned}
\tag{37}
$$

As a check, we compare the extracted angles with the standard formula for Collins-Soper [20] CM frame lepton decay angle, $\cos\theta$, which is:

$$
\cos\theta = \frac{2}{M\sqrt{M^2+P_{\mathrm{T}}^2}}(\ell_1^+\ell_2^- - \ell_1^-\ell_2^+) \tag{38}
$$

where M is the mass of the dielectron pair, $\ell_1(\ell_2)$ is the four-momentum of electron (positron), P_{T} is the transverse momentum of the electron-positron pair, and $\ell^{\pm}$ corresponds to $\frac{1}{\sqrt{2}}(\ell^0 \pm \ell^3)$.

References

[1] E. Mirkes, Nucl. Phys. B **387** 3, (1992).

[2] W and Z polarization effects in hadronic collisions. E. Mirkes , J. Ohnemus, Phys. Rev. **D50**:5692-5703 (1994).

[3] Angular distributions of Drell-Yan lepton pairs at the Tevatron: Order α_s^2 corrections and Monte Carlo studies. E. Mirkes , J. Ohnemus, Phys. Rev. **D51**:4891-4904 (1995). e-Print: hep-ph/9412289

[4] Study of the angular coefficients and corresponding helicity cross sections of the W boson in hadron collisions. John Strologas, Steven Errede, Phys. Rev. **D73**:052001 (2006).

[5] Measurement of the Differential Angular Distribution of the W Boson produced in association with Jets in Proton - Anti-proton Collisions center-of-mass energy = 1.8-TeV. John Strologas, (Illinois U., Urbana) . FERMILAB-THESIS-2002-47, UMI-30-70054, Dec 2002. 259pp. Ph.D. Thesis (Advisor: Steven Errede).

[6] J. C. Collins, Phys. Rev. Lett. **42**, 291 (1979); Daniel Boer and Werner Vogelsang, Phys. Rev. **D74**:014004 (2006).

[7] Edmond L. Berger,, Jian-Wei Qiu, , Ricardo A. Rodriguez-Pedraza, Phys. Rev. **D76**:074006 (2007): Edmond L. Berger , Jian-Wei Qiu, Ricardo A. Rodriguez-Pedraza, Phys. Lett. **B656** (2007).

[8] W production in an improved parton shower approach. Gabriela Miu, Torbjorn Sjostrand, Phys. Lett. **B449**:313-320 (1999).

[9] A simple event weighting technique for optimizing the measurement of the forward-backward asymmetry of Drell-Yan dilepton pairs at hadron colliders. Arie Bodek, e-Print: arXiv:0911.2850 [hep-ex]

[10] J. Lindfors, Physica Scripta **20**, 19 (1979).

[11] T. Sjöstrand et al., Comput. Phys. Commun. **135**, 238 (2001). PYTHIA 6.2: hep-ph/0108264.

[12] T. Sjöstrand et al., JHEP **05**, 026 (2006). PYTHIA 6.4: hep-ph/0603175.

[13] H.L. Lai et al., Eur. Phys. J. **C12**, 375 (2000).

[14] F. Abe et al., Phys. Rev. Lett. **84**, 845 (2000).

[15] F. Abe et al., Phys. Rev. **D63**, 011101R (2000).

[16] J.-Y. Han, A. Bodek, Y.S. Chung, W.K. Sakumoto, CDF note 9832: "Measurement of $d\sigma/dy$ of Drell-Yan e^+e^- Pairs in the Z Mass Region from $p\bar{p}$ Collisions at $\sqrt{s}$ =1.96 TeV". Supporting CDF notes: 9142, 9513, 9755, and 9792.

[17] T. Aaltonen et al. (CDF Collaboration), hep-ex/0908.3914.

[18] G.A. Ladinsky and C.-P. Yuan, Phys. Rev. **D50** 4239 (1994); C. Balazs and C.-P. Yuan, Phys. Rev. **D56**, 5558 (1997); F. Landry, R. Brock, P.M. Nadolsky, and C.-P. Yuan, Phys. Rev. **D67** 073016 (2003).
Additional details: `http://hep.pa.msu.edu/resum`.
Code: cpy_113009 ($\sin^2\theta_W = 0.2314$);
Grid files: dy_*_tev2_ct66 w321.00 and yk.00.

[19] R.K. Ellis and S. Veseli, Nucl. Phys. **B511**, 649 (1998). The calculation uses CTEQ6M PDFs (J. Pumplin et al., JHEP07, 012 (2002), hep-ph/0201195) and PYTHIA's default Z–fermion EWK coupling of $\sin^2\theta_{\rm W} = 0.232$.

[20] J.C. Collins and D.E. Soper, Phys. Rev. **D16**, 2219 (1977).

[21] The CDF EWK/TOP standard tune parameters for PYTHIA's W/Z $P_{\rm T}$ are: MSTP(91)=1, PARP(91)=2.10, and PARP(93)=15 for the low $P_{\rm T}$ Gaussian smearing, with PARP(62)=1.25 and PARP(64)=0.2 for the $P_{\rm T}$ evolution in the 7–25 GeV region.

[22] J. Pumplin, D.R. Stump, J. Huston, H.L. Lai, P. Nadolsky, W.K. Tung, JHEP 0207 (2002) 012.

[23] P M.Nadolsky et al. (CTEQ collaboration) Phys. Rev. **D78**:013004 (2008).

[24] A.D. Martin, R.G. Roberts, W.J. Stirling, and R.S. Thorne, Eur. Phys. J. **C28**, 455 (2003).

[25] A.D. Martin, W.K. Stirling, R.S. Thorne, and G. Watt, Phys. Lett. **B652**, 292 (2007).

[26] A simple event weighting technique for optimizing the measurement of the forward-backward asymmetry of Drell-Yan dilepton pairs at hadron colliders. Arie Bodek, e-Print: arXiv:0911.2850 [hep-ex]